Jussila, Topias; Philip, Anish; Rubio-Giménez, Víctor; Eklund, Kim; Vasala, Sami; Glatzel, Pieter; Lindén, Johan; Motohashi, Teruki; Karttunen, Antti J.; Ameloot, Rob; Karppinen, Maarit

Chemical Bonding and Crystal Structure Schemes in Atomic/Molecular Layer Deposited Fe-Terephthalate Thin Films

Published in:
Chemistry of Materials

DOI:
10.1021/acs.chemmater.4c00555

Published: 09/07/2024

Document Version
Publisher's PDF, also known as Version of record

CHEMISTRY OF MATERIALS

pubs.acs.org/cm

Article

Chemical Bonding and Crystal Structure Schemes in Atomic/Molecular Layer Deposited Fe-Terephthalate Thin Films

Published as part of Chemistry of Materials virtual special issue "C. N. R. Rao at 90".

Topias Jussila, Anish Philip, Víctor Rubio-Giménez, Kim Eklund, Sami Vasala, Pieter Glatzel, Johan Lindén, Teruki Motohashi, Antti J. Karttunen, Rob Ameloot, and Maarit Karppinen*

Cite This: *Chem. Mater.* 2024, 36, 6489–6503

Read Online

ACCESS | Metrics & More | Article Recommendations | Supporting Information

ABSTRACT: Advanced deposition routes are vital for the growth of functional metal–organic thin films. The gas-phase atomic/molecular layer deposition (ALD/MLD) technique provides solvent-free and uniform nanoscale thin films with unprecedented thickness control and allows straightforward device integration. Most excitingly, the ALD/MLD technique can enable the in situ growth of novel crystalline metal–organic materials. An exquisite example is iron-terephthalate (Fe-BDC), which is one of the most appealing metal–organic framework (MOF) type materials and thus widely studied in bulk form owing to its attractive potential in photocatalysis, biomedicine, and beyond. Resolving the chemistry and structural features of new thin film materials requires an extended selection of characterization and modeling techniques. Here we demonstrate how the unique features of the ALD/MLD grown in situ crystalline Fe-BDC thin films, different from the bulk Fe-BDC MOFs, can be resolved through techniques such as synchrotron grazing-incidence X-ray diffraction (GIXRD), Mössbauer spectroscopy, and resonant inelastic X-ray scattering (RIXS) and crystal structure predictions. The investigations of the Fe-BDC thin films, containing both trivalent and divalent iron, converge toward a novel crystalline Fe(III)-BDC monoclinic phase with space group $C2/c$ and an amorphous Fe(II)-BDC phase. Finally, we demonstrate the excellent thermal stability of our Fe-BDC thin films.

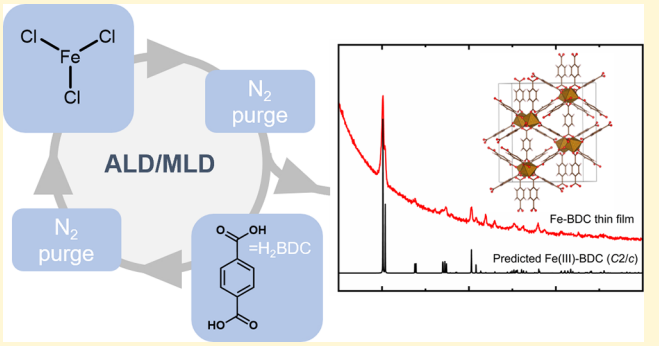

1. INTRODUCTION

Pushing the boundaries of materials may convey solutions to the compelling global challenges including clean water supply, sustainable energy production, and the use of sustainable materials resources. To enrich the new material/new property platform, one of the leading strategies is to combine inorganic and organic components into a single (multi)functional material;[1] a prime example is the rapidly expanding family of so-called metal–organic framework (MOF) materials with their diverse functional properties.[2,3] So far these exciting hybrid materials have been mainly synthesized in powder form, but lately, increasing efforts have focused on producing these materials in thin-film form, to expedite the journey from the fundamental material research to industry-feasible production and integration into the targeted device configuration.[4] The leap from the bulk to thin films imposes both challenges and opportunities: New robust deposition techniques are a necessity to surpass the common bottleneck of available advanced thin-film fabrication routes. On the other hand, the thin films may possess completely new compositional/structural features and thus new functional properties as well. Unveiling those novel features can be highly demanding, and hence an extended toolbox of characterization and modeling techniques must be established.

In recent years, the atomic/molecular layer deposition (ALD/MLD) technique, based on gaseous/vaporized precursors, has strongly emerged as an attractive alternative for the conventional solution-based fabrication techniques (adopted from corresponding bulk-material synthesis methods) for various inorganic–organic hybrid materials in thin-film form.[5,6] This technique is similar in fundamentals to the ALD (atomic layer deposition) technique—the fastest growing thin-film technology in the microelectronics industry and beyond for several decades already. The difference between the two techniques is that while in ALD purely inorganic thin films are grown from inorganic precursors (e.g., $FeCl_3$ + H_2O for Fe_2O_3 thin films), in ALD/MLD the second precursor (co-

Received: February 27, 2024
Revised: June 10, 2024
Accepted: June 10, 2024
Published: June 25, 2024

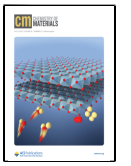

reactant) is replaced with an organic precursor (e.g., $FeCl_3$ + HOOC−C_6H_4−COOH for Fe-terephthalate thin films). Another way to describe the ALD/MLD technique is to consider it as a hybrid between ALD and its less-exploited MLD (molecular layer deposition) counterpart for purely organic thin films grown from two different organic precursors.

Common to all three of these techniques, ALD, ALD/MLD, and MLD, is that they can produce high-quality, pinhole-free, large-area homogeneous, and conformal thin films and coatings even on challenging substrates with atomic/molecular level precision but yet in an industry-feasible fashion.[5,7,8] These attractive attributes are derived from the self-terminating gas-surface reactions and the unique precursor feeding sequence in which the two (or more) different precursors are individually pulsed into the reactor chamber separated by an inert gas purge. Numerous ALD/MLD processes have been developed for, e.g., magnetic,[9−11] optical,[12−15] thermoelectric,[16,17] bioactive,[18,19] electrochemical,[20−25] and barrier/encapsulation[26−28] applications. Chemistry-wise, these materials cover most of the s-block and 3d transition metals, lanthanides, and some p-block and 4d and 5d transition metals, together with a variety of organic moieties from simple alkyls (e.g., ethylene glycol) to more complex aromatic molecules (e.g., azobenzene-4,4-dicarboxylic acid or 9,10-anthracenedicarboxylic acid),[29,30] and even natural organics (e.g., nucleobases or curcumin).[18,31]

An exciting milestone in ALD/MLD research was the demonstration that the technique enables—besides new attractive amorphous metal−organic materials—the deposition of in situ crystalline thin films of various metal−organics: the first report is for porous Cu-BDC (BDC = 1,4-benzenedicarboxylate; terephthalate) MOF-2 thin films grown from $Cu(thd)_2$ (thd = 2,2,6,6-tetramethyl-3,5-heptanedione) and H_2BDC (1,4-benzenedicarboxylic acid; terephthalic acid) precursors.[32−34] Later many reports on in situ crystalline ALD/MLD materials have followed, mainly for alkaline[35] and alkaline earth[36] metals but for transition metals[37,38] as well. Even more impressive is the fact that the gas-phase synthesis allows us to stabilize entirely new compounds and crystal structures not known before.[29,39,40] The first ALD/MLD example was lithium-quinone,[41] which was later shown to be a promising cathode material for an all-ALD/MLD-made Li-organic microbattery.[20] A more recent prominent example is the iron-terephthalate (Fe-BDC) thin films grown from simple precursors ($FeCl_3$ and H_2BDC) at relatively low deposition temperatures (240−300 °C) without any specific requirements for the substrate material.[42]

Owing to its simple and critical-element-free composition and diverse property palette, the Fe-BDC system has indeed been considered an attractive functional material for many next-generation applications. Several different forms of Fe-BDC have been synthesized and thoroughly investigated in bulk form: Figure 1 shows yearly publications (Web of Science) related to Fe-BDC and its derivatives. In the last 15 years, nearly 1000 papers have been published about this material, most of the studies involving solvothermally synthesized bulk Fe-BDC samples. For these samples, several crystal phases have been identified, including MIL-53(Fe), MIL-235(Fe), MIL-101(Fe), and MIL-88B(Fe). Which structure is formed depends on the synthesis conditions and the exact chemical composition of the product. Essentially all of the Fe-MIL structures contain solvent molecules (e.g., *N*,*N*-dimethylformamide; DMF) or other guest moieties (e.g., OH^- or Cl^-) as an integral part of the structure.[43]

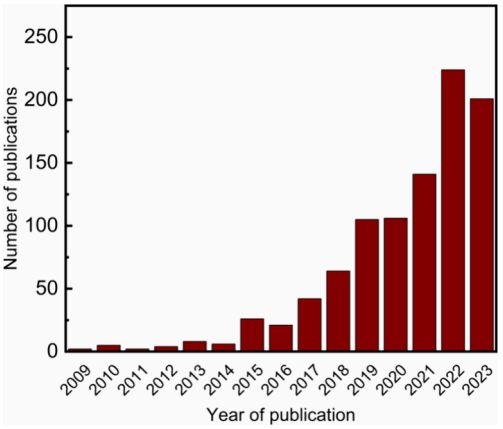

Figure 1. Yearly publications for iron-terephthalate MOFs. The data were extracted from Web of Science on November 21, 2023. The following search words were used: iron-terephthalate, Fe-BDC, MIL-53(Fe), MIL-235(Fe), MIL-101(Fe), MIL-88B(Fe).

A great deal of the Fe-BDC publications concern photocatalytic properties relevant to waste treatment processes (e.g., oxidation of organic dyes, reduction of poisonous metals)[44−46] and colorimetric biosensing properties, which are pivotal for a range of applications especially in the medical industry (detection of cancer cells, drug molecules, etc.).[47−50] Moreover, the excellent adsorption and desorption capabilities of Fe-BDC MOFs, induced by the specific ordered and porous structures, are attractive for, e.g., drug delivery, gas separation, and lithium-ion battery solutions.[51−54] In practice, many of the applications would require Fe-BDC thin films, which have so far been challenged only through solution-based thin-film fabrication techniques,[51,52,55−59] incompatible with industry standards. A more appealing method would be to grow the thin films directly on a substrate from gaseous precursors using the ALD/MLD technique.[42,60]

The ALD/MLD process for the Fe-BDC thin films is schematically illustrated in Figure 2. Since the process does not involve any solvents and all the gas-phase byproducts (such as HCl) are removed from the reaction chamber during the purging steps, chemical compositions/bonding schemes and crystal structures different from the widely studied solution-synthesized iron-terephthalates can be anticipated. Thorough investigation of these features, however, is not straightforward or possible via conventional methods due to the extremely small material amounts and the need of a supporting structure.

Here we will demonstrate—using an extensive combination of advanced thin-film characterization techniques and computational modeling (Figure 2)—that the ALD/MLD grown Fe-BDC thin films indeed exhibit novel chemical and structural features. Interestingly, the films are found to contain both tri- and divalent iron; for the Fe(III)-BDC phase a novel monoclinic crystal structure (space group *C*2/*c*) is discovered, while the Fe(II)-BDC phase seems to exist in the films in an amorphous form. These findings underline the possibility to use gas-phase synthesis to create hybrid materials that are fundamentally different from the related solution-synthesis products and provide a successful recipe for discovering the composition and structure for such new metal−organic thin-film materials with no bulk counterpart.

https://doi.org/10.1021/acs.chemmater.4c00555
Chem. Mater. 2024, 36, 6489−6503

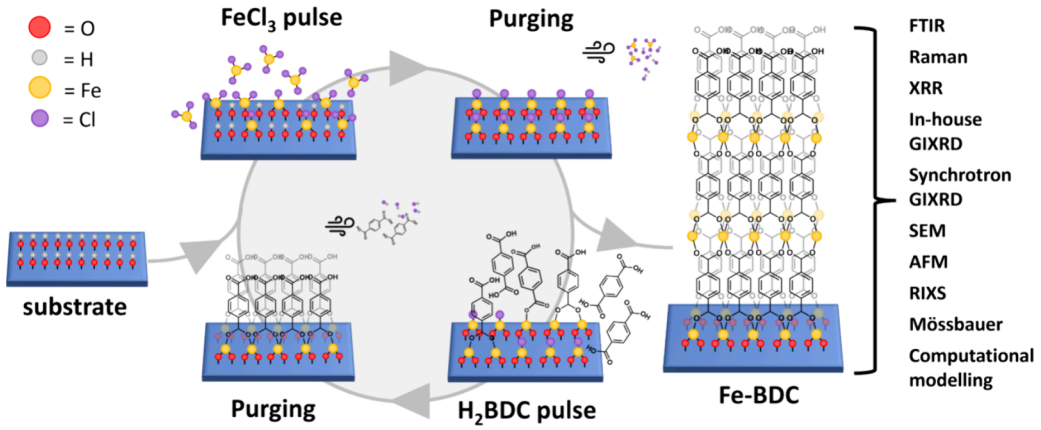

Figure 2. ALD/MLD process for Fe-BDC: gaseous $FeCl_3$ and H_2BDC precursors are pulsed into the reaction chamber one at a time, separated by inert N_2 gas purge to remove excess precursors and reaction byproducts. Characterization methods employed in this work for the resultant in situ crystalline Fe-BDC thin films are listed on the right.

2. EXPERIMENTAL SECTION

2.1. Thin Film Depositions. The Fe-BDC thin films were deposited using a flow-type hot-wall ALD reactor (F-120 by ASM Microchemistry Ltd.) as previously reported,[42] by pulsing $FeCl_3$ (Merck, 95%; 155 °C) and H_2BDC (Tokyo Chemical Industry CO., Ltd., >99.0%; 185 °C) precursors according to the following sequence: 4 s ($FeCl_3$)/8 s (purge)/20 s (H_2BDC)/40 s (purge). In this work, the investigated deposition temperature range was 210−300 °C. The depositions were carried out on 3 × 3 cm^2 Si(100) wafers (without removing the native oxide layer) or Kapton (polyimide) substrates. The reactor pressure was kept around 5 mbar, while N_2 gas flow (300 SCCM) was used for both pulsing and purging.

2.2. Sample Characterization. Fourier transform infrared (FTIR; Bruker alpha II) and Raman (Renishaw inVia Confocal Raman Microscope) spectroscopy measurements were performed at room-temperature (ambient conditions) in transmittance mode (400−4000 cm^{-1}) and reflectance mode (100−3400 cm^{-1}), respectively, to study the composition and bonding of the films. The Si substrate contribution was subtracted from the FTIR data. For thermal stability measurements, in situ FTIR measurements were performed by employing a diffuse reflection method (JASCO FT/IR-4700) using a DLATGS detector (with Peltier temperature control) and in situ measurement chamber (JASCO DR-650Ai) at gradually elevated temperatures either using N_2 flow or sealing the sample compartment with air inside. The initial reference spectrum was recorded at 40 °C, and the following spectra were recorded for the same sample after each consequent heat-treatment step at 100 °C intervals in the 100−600 °C range. Finally, after cooling down the sample, the last spectrum was recorded at 40 °C. In these experiments, the heating rate was 20 °C/min, and the sample was kept at each temperature for 20 min during which the FTIR spectrum was recorded three times (at 0, 10, and 20 min). Additional thermal stability measurements were performed by heating the thin film samples in a regular open furnace and then measuring FTIR spectra (Bruker alpha II) and film thickness.

Film morphology was investigated with both scanning electron microscopy (SEM; Tescan Mira 3; 20.0 kV acceleration voltage) and atomic force microscopy (AFM; Bruker MultiMode 8 AFM; NanoScope Analysis 3.00 software), carried out on 2 × 2 μm^2 area in ScanAsyst mode with auto adjustment of key parameters (e.g., feedback gain), scan rate of 1 Hz, and scan resolution of 512 × 512 pixels. X-ray reflectivity (XRR; X'Pert MPD PRO Alfa 1 PANalytical) was measured using a sealed proportional detector (PW3011/20) and a fixed divergence slit (1/32°). A Cu attenuator was used in the initial steps of the measurements to protect the detector from excess X-ray exposure and manually removed after sufficient intensity drop for improved data quality at higher incident angles. The XRR data were fitted using X'Pert Reflectivity software (PANalytical) to obtain the film thickness and estimate the film density and roughness. The same equipment was used for in-house GIXRD (Cu $K\alpha_1$ radiation) measurements in the 2θ range of 5−60° and with a fixed incidence angle of 0.65°. A fixed divergence slit (1/2°) was used together with a 10 mm beam mask.

Synchrotron GIXRD measurements were performed at the I07 beamline of Diamond Light Source (λ = 0.99 Å; Didcot, United Kingdom) using a stationary Pilatus 2M detector. Thin film samples were placed on holders mounted on a multiaxis diffractometer at a sample-to-detector distance of 388 mm (calibrated with a LaB_6 reference sample). Pixel images were acquired at an incidence angle of 0.25° and then processed into diffractograms using the GIDVis software package.[61]

^{57}Fe Mössbauer measurements (300 K) were performed in transmission geometry using a two-year-old 50 mCi Co-57(Rh) source from Rietverc Co. A linear Doppler velocity with a maximum velocity of 4.0 mm/s was used. The absorbers (samples) were made by cutting the films deposited on Kapton tape in circular pieces with a diameter of 18 mm and stapling them on top of each other to get a stack of 60−80 layers (total Fe-BDC film thickness appr. 18−24 μm). The spectra were fitted using a homemade nonlinear least-squares fit program, with the full Hamiltonian of mixed electric and magnetic interaction. Fit parameters were the quadrupole-coupling constant (eQV_{zz}), isomer shift (δ), component intensities (I), and experimental line-width (Γ) constrained equal for all components.

Resonant inelastic X-ray scattering measurements were carried out at beamline ID26 of the European Synchrotron Radiation Facility (ESRF) in Grenoble, France. Information was collected at the Fe 1s2p RIXS planes. The first harmonic of the undulator source was used, and the incident energy was selected and monochromatized by a pair of Si(311) crystals. The emission energy was scanned using a point-to-point Johann spectrometer; five spherically bent analyzer crystals with Ge(440) reflections were used to select the emission energy, together with an avalanche photodiode detector.[62] The RIXS planes were recorded by stepping through the emission energy range and scanning the incident energy at each step. Slight beam damage was found with exposure times longer than 30 s. To avoid the damage, the scan time was set to 20 s, the sample was moved between each scan, and a concentration correction scan was done after recording the RIXS plane.

The Fe 1s2p RIXS planes were simulated using the crystal field multiplet code Quanty[63] together with the Crispy[64] user interface. Calculations were done for different Fe oxidation states and local point-group symmetries. Atomic Hamiltonian scaling factors, crystal field energies/parameters, and peak broadening parameters were adjusted to best fit the experimental data. In the RIXS planes, the data are plotted as a two-dimensional graph, with incident energy (IE) on

https://doi.org/10.1021/acs.chemmater.4c00555
Chem. Mater. 2024, 36, 6489−6503

the x-axis and energy transfer (ET) on the y-axis. The intensity is normalized to the pre-edge feature maximum.

2.3. Computational Modeling. Crystal structure predictions for the search of the most probable crystal structure of Fe-BDC were carried out with both Fe(II) and Fe(III) using quantum chemical methods and the USPEX[65−67] (version 9.4.4) evolutionary algorithm. In the evolutionary searches, interfaces with two quantum chemical codes, CRYSTAL17[68]/23[69] and DFTB (version 22.2),[70] were used. USPEX combined with CRYSTAL has previously been used to investigate, for example, the ground state structures of different known and unknown magnetic d-metal oxides,[71,72] novel synthesized fluorides,[73] as well as novel dilithium 2-aminoterephthalate material obtained through ALD/MLD.[74] Evolutionary structure search was complemented with the investigation of known d-metal MOF structures: $Sc(III)_2$-BDC_3,[75] Cu(II)-BDC MOF-2,[76] and Co(II)-BDC MOF-71.[77]

In total thousands of structures were investigated using different numbers of formula units (Z) and two quantum chemical codes interfaced with the algorithm. In CRYSTAL calculations, PBE0 hybrid density functional method (DFT-PBE0) was used. In DFTB calculations, the GFN1-xTB Hamiltonian was used.[78] Two molecular building blocks were used in the USPEX evolutionary searches: Fe atom [Fe(III) or Fe(II)] and BDC anion, $C_6H_4(CO_2)_2^{2-}$. The USPEX input files and the molecular building blocks are given in the Supporting Information. The oxidation state of Fe was set by balancing the number of BDC molecular building blocks with respect to that of Fe atoms, with a Fe:BDC ratio of 2:3 for Fe(III) and 1:1 for Fe(II). Mixed Fe(II)−Fe(III) structures were studied with a Fe:BDC ratio of 3:4. Both antiferromagnetic and ferromagnetic spin configurations of the Fe atoms were evaluated in CRYSTAL calculations. Ferromagnetic structures were found to be energetically more favorable. Evolutionary searches with the CRYSTAL code did not produce sufficiently matching structures with respect to experimental data, and the computationally less demanding semi-empirical DFTB code was additionally used for investigations, with reoptimization of structures always carried out with CRYSTAL (DFT-PBE0 method and ferromagnetic spin ordering).

For Fe(III), the simplest stoichiometric composition is $Fe_2(C_6H_4(CO_2)_2)_3$. With USPEX/CRYSTAL one run was carried out for Fe(III) with Z = 1 (50 atoms) and one with Z = 2. Two further runs each were carried out with USPEX/DFTB using compositions Z = 1 and Z = 2. For Fe(II), with stoichiometric composition $Fe(C_6H_4(CO_2)_2)$, two USPEX runs each for compositions Z = 2 (34 atoms) and Z = 4 were carried out. One run was further conducted for the mixed Fe(II)−Fe(III) case, with 2 Fe(III) and 1 Fe(II), $Fe_3(C_6H_4(CO_2)_2)_4$ (67 atoms). Evolutionary searches with larger numbers of formula units (Z) often failed to produce any low-energy structures and resulted in low-symmetry structures, in line with our previous experiences. The lowest-energy structures from the evolutionary searches were all reoptimized with CRYSTAL using default optimization criteria in the final structural optimizations, the DFT-PBE0 method, and the TZVP basis for H, C, and O[79] and SVP for Fe,[80] derived from molecular Karlsruhe basis sets.[81] USPEX input parameters are included in the Supporting Information, along with further computational details such as the used Monkhorst−Pack-type k-meshes.

Harmonic frequency calculations at the Γ-point were carried out with CRYSTAL to confirm the studied structures as true local minima and to obtain the theoretical IR and Raman spectra.[82−85] For the simulation of the IR spectra, a Lorentzian line shape with a FWMH of 8 cm^{-1} was used. For the Raman spectra a pseudo-Voigt band profile (50:50 Lorentzian/Gaussian) with a fwhm of 8 cm^{-1} was used. Investigation of the normal modes was carried out visually with the CRYSPLOT tools.[86]

3. RESULTS AND DISCUSSION

3.1. Deposition of Fe-BDC Thin Films. In our original report on the ALD/MLD growth of in situ crystalline Fe-BDC thin films,[42] limited attention was paid to the effect of deposition temperature on the growth rate (growth-per-cycle; GPC), density, and film morphology. Thus, these characteristics are discussed in more detail here. First, as seen in Figure 3, the GPC is around 1 nm/cycle for the entire range of

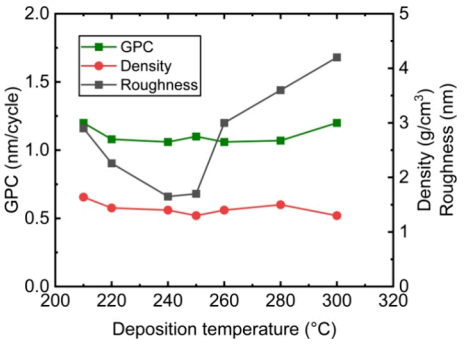

Figure 3. GPC, film density, and root-mean-square roughness values determined from XRR data for Fe-BDC thin films deposited at different temperatures (film thicknesses ca. 50 nm).

deposition temperatures investigated. This is significantly (10×) higher than for other ALD/MLD grown 3d metal-BDC thin films for which the GPC value is in the scale of 1 Å/cycle.[87] We believe that the main reason for the high growth rate of the Fe-BDC films is the highly reactive and small $FeCl_3$ precursor. For the other 3d metal-BDC thin films, larger metal β-diketonate precursors with less reactive metal−oxygen coordination have been used; the bulky diketonate ligands in these precursors cause steric hindrance by blocking the nearby surface reaction sites, thus lowering the growth rate. Another interesting difference is that, for the present $FeCl_3$ + H_2BDC process, the GPC remains essentially independent of the deposition temperature, while the GPC of H_2BDC-based ALD/MLD processes typically decreases with increasing deposition temperature due to increased precursor desorption on the substrate surface.[32,87] We believe that with the highly reactive $FeCl_3$ precursor the reaction occurs fast and efficiently at all temperatures, such that the increased desorption rate at higher temperatures becomes insignificant.

The density of our Fe-BDC films also remains relatively stable (1.3−1.5 g/cm^3) throughout the deposition temperature range. The density values are similar to the ALD/MLD grown crystalline (MOF-2) Cu-BDC[33] thin films as well as with amorphous Ni-BDC[87] thin films (1.4 g/cm^3). In contrast, the film roughness clearly depends on the deposition temperature: first the roughness decreases from 210 to 240 °C and then increases from 250 to 300 °C. These trends are obvious also from the visual observation of the XRR patterns (shown in Figure S1), as the decay rate of the Kiessig oscillations, which is proportional to the film roughness due to scattering effects, first decreases and then increases with increasing deposition temperature. The same trend and very similar roughness values were extracted from AFM measurements (Figure S2). The slightly higher roughness values seen at the lowest deposition temperatures (210−220 °C) could result from the fact that these temperatures are very close to the sublimation temperature (185 °C) of the H_2BDC precursor, which can lead to partial precursor condensation on the substrate and thus nonideal film growth through gas-phase reactions. This would explain also the slightly higher GPC at 210 °C. Once the deposition temperature is increased to 240 °C, the risk of condensation is already low. Then, from 250 to 300 °C, the

https://doi.org/10.1021/acs.chemmater.4c00555
Chem. Mater. 2024, 36, 6489−6503

increasing roughness is attributed to an increasing grain size; from SEM images (Figure S3) performed for thicker (~300 nm) Fe-BDC films an increase of average grain size from ~150 nm (250 °C) to ~400 nm (300 °C) and a change in the grain shape from rounded to platelet-like particles were revealed. These results are supported by AFM measurements performed for the thicker films (Figure S4).

3.2. Bonding Scheme. The chemical composition and bonding scheme in the Fe-BDC films were studied via FTIR and Raman spectroscopy (Figure 4). First of all, no major deposition-temperature-dependent changes implying chemical composition changes were found in these spectra. In the FTIR spectra, the characteristic C−H out-of-plane bending (739 cm^{-1}) and ring stretch (1425 cm^{-1}, 1505 cm^{-1}) vibration modes of the aromatic backbone[46,88,89] are clearly discerned. Also, the characteristic Fe−O bonding feature due to iron atoms bonded to the carboxylate group (COO^-) is found as expected at 523 cm^{-1}.[89] In the Raman spectra, the characteristic C═C stretch at 1612 cm^{-1} and the C−H out-of-plane bending at 868 cm^{-1} verify the existence of the aromatic backbone; in addition, the C−C bond stretch between the aromatic carbon and carbon of the carboxylate group is seen at 1148 cm^{-1}.[89,90]

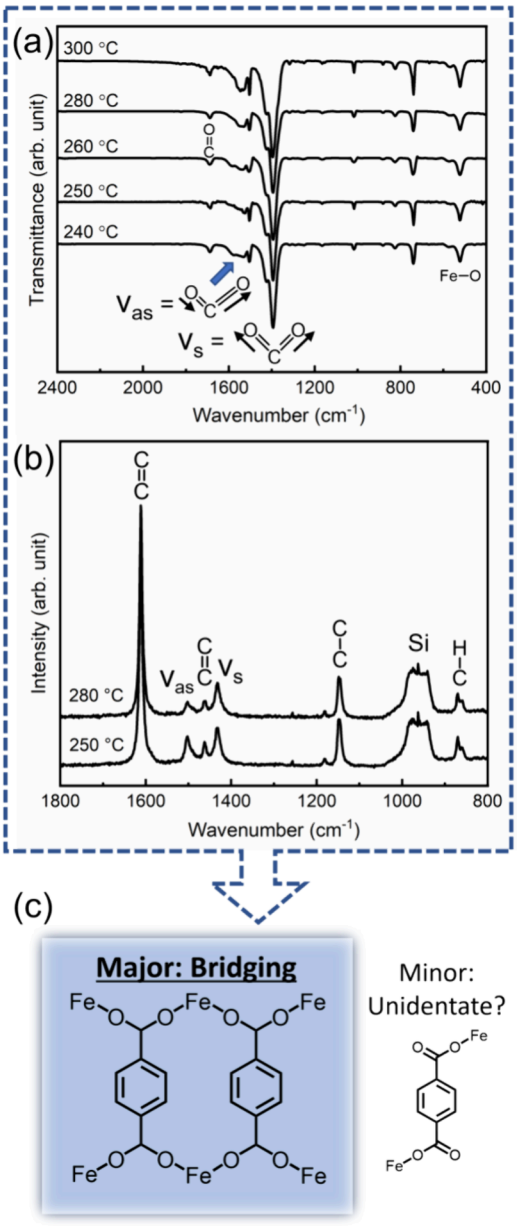

Figure 4. Room-temperature (a) FTIR and (b) Raman spectra of Fe-BDC thin films (thicknesses ~350 nm) for indicated deposition temperatures. (c) Bonding modes between iron and carboxylate groups deduced from the FTIR and Raman spectra; the bridging mode is found to be the main bonding mode, but residual unidentate bonding is possible as well.

For the bonding scheme, the most informative FTIR spectral range is the 1300−1700 cm^1 region consisting of the symmetric (ν_s) and asymmetric vibration (ν_{as}) modes of the carboxylate (COO^-) group: the splitting (Δ) between these peaks provides information on the Fe−OCO−Fe bonding mode.[91,92] For the Fe-BDC films, the characteristic ν_s is clearly observed at 1394 cm^{-1}, while the less-intensive ν_{as} is located around 1580 cm^{-1}. The thus obtained Δ value of ~186 cm^{-1} is indicative of bridging type Fe−OCO−Fe bonding which is sketched in Figure 4(c).[91] It should be noted that, in our original Fe-BDC report,[42] the IR 1504 cm^{-1} feature was erroneously assigned to ν_{as}, and accordingly a bidentate bonding type was concluded. However, based on previous similar observations for other ALD/MLD grown Fe and/or H_2BDC based inorganic−organic thin films and also for reported bulk Fe-BDC samples[32,46,87,89,93,94] and the fact that the 1504 cm^{-1} is highly characteristic for most aromatic-based materials, we are now convinced that the ν_{as} is located around 1580 cm^{-1}. Moreover the bridging mode is preferred especially for 3-dimensional periodic (crystalline) networks.[32,95] Finally, we note that the ν_s and ν_{as} Raman signals of COO^- are observed at 1432 and 1503 cm^{-1}, respectively.[89,96]

It should be emphasized that the assignment of IR vibrations is often ambiguous; especially here the ν_{as} severely overlaps with the ring stretch vibration modes, making the precise assignment uncertain. Moreover, the IR frequency of ν_{as} depends on the oxidation state of the metal,[97] and as demonstrated below, the Fe(III)/Fe(II) ratio in our Fe-BDC films decreases with increasing deposition temperature. This most likely causes the overlapping peaks around 1580−1550 cm^{-1} to shift to some extent (~30 cm^{-1}) with the changing deposition temperature.

In addition to the ν_s and ν_{as} COO^- vibrations observed for the bridging mode, a relatively small but still clearly visible IR signal at 1690 cm^{-1} is observed. This is a strong sign of carbonyl groups, present in the sample due to some unreacted H_2BDC precursor molecules or unidentate Fe−OOC bonding type [Figure 4(c)]. The unreacted COOH groups would be expected to show O−H stretching features above 3000 cm^{-1} which are not visible in the present spectra (IR; Figure S5). If the 1690 cm^{-1} signal originates from the unidentate Fe−OOC bonding, it is nevertheless a minor secondary bonding type in our Fe-BDC films where the bridging-type bonding dominates. Indeed, the carbonyl signal was only seen for the 350 nm thick films (spectra shown in Figure 4), while it was nearly invisible for the thinner films.

3.3. Iron Oxidation State. The local and electronic structures (oxidation states) of iron atoms in our Fe-BDC films were first studied via RIXS measurements. Figure 5(a) shows the measured Fe 1s2p RIXS plane in the K-absorption pre-edge region. The measured spectrum consists of two groups of features, i.e., lower ET [706−712 eV; Ka_1 ($2p_{3/2}$)] and higher ET [719−725 eV; Ka_2 ($2p_{1/2}$)] areas, both split by ~13 eV due

https://doi.org/10.1021/acs.chemmater.4c00555
Chem. Mater. 2024, 36, 6489−6503

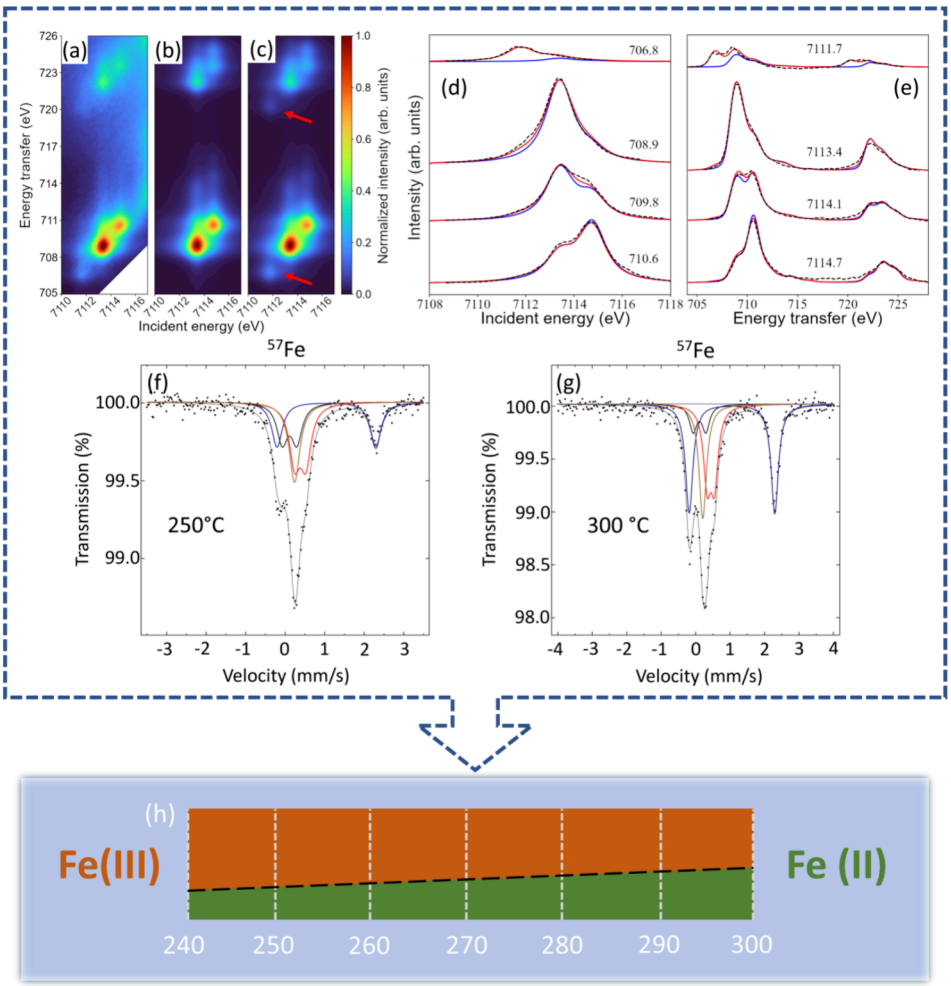

Figure 5. (a) Experimental RIXS plane of Fe-BDC thin film deposited at 280 °C. Calculated RIXS plane for (b) Fe(III) in octahedral coordination and (c) 80% Fe(III) and 20% Fe(II) both in octahedral coordination; the Fe(II) component is emphasized with a red arrow in the calculated plane. (d) CET and (e) CIE cuts of the experimental Fe-BDC (black dashed line), calculated Fe(III) (blue solid line), and calculated combined 80% Fe(III) + 20% Fe(II) (red solid line) RIXS planes. All Fe components are in octahedral coordination. The numbers indicate the energies (eV) at which the cuts were made. (f, g) Mössbauer spectra of Fe-BDC thin films deposited at 250 and 300 °C. The blue line is due to Fe(II), while the light brown and red lines are due to Fe(III) species. The black line originates from traces of iron in the beryllium window of the detector, and it is independent of the sample being measured. (h) Schematic summary of the decreasing Fe(III)/Fe(II) ratio with increasing deposition temperature based on the combined information from Mössbauer and RIXS analyses.

to the 2p spin−orbit coupling. A close-up of the Ka_1 region is shown in Figure S6(a). The pre-edge features are well separated from the main K absorption edge. In the lower ET area, there are two clear maxima at (7113.4 eV IE, 708.9 eV ET) and at (7114.7 eV IE, 710.6 eV ET), associated with the t_{2g} and e_g orbitals (split by crystal field), respectively. These features are in reality split even further because of multiplet effects, but due to the lifetime and experimental broadenings, the splitting is obscured and only the two broad features are seen.

The strong signals are similar to that of $Fe(acac)_3$ with an octahedral Fe(III),[98] but an additional weak feature at the lower energy (7111.7 eV IE, 706.8 eV ET) is observed as well. This is assumed to originate from Fe(II).[98] Figure 5(b) shows the calculated RIXS plane with only the octahedral Fe(III) component, while Figure 5(c) shows the calculated RIXS plane with 80% Fe(III) and 20% Fe(II), both octahedral. The close-ups of the calculated Ka_1 region are shown in Figure S6(b,c). Evidently, the Fe(II) component is required to model the measured spectrum completely (red arrows).

To validate this observation and properly compare the experimental and calculated spectra, cuts along the constant energy-transfer [CET; Figure 5(d)] and constant incident energy [CIE; Figure 5(e)] (L2,3-edge like) were performed. As the calculated energies are not absolute values, the spectra were shifted to match the experimental ones. First, the CET and CIE cuts were calculated only for Fe(III). Here the important relative features and best fit parameters were 10Dq = 1.35 eV, Fk = 0.6, Gk = 0.7, and SOC = 1 of Hartree−Fock values. In addition, 0.4/0.9 eV Gaussian broadening was added. The Fe(III) is in the high-spin state. As shown in Figure 5(d) and (e), with these Fe(III) parameters (blue line) the main (high-energy) features of the experimental RIXS plane match well.

However, the low energy feature (7111.7 eV IE, 706.8 eV ET) is reproduced only when Fe(II) is added to the fitting (red line). The addition of Fe(II) also completes a bit of missing intensity to the main features. Due to the relatively weak signal of the Fe(II) component, it is overlapped by the main Fe(III) features. The exact parameters for Fe(II) could

https://doi.org/10.1021/acs.chemmater.4c00555
Chem. Mater. 2024, 36, 6489−6503

not be determined, so a bit smaller 10Dq = 1.2 eV (typically smaller for lower oxidation states) was used, although it has little impact on the fit. The rest of the parameters are the same as for Fe(III), and all the Fe components are in the high-spin state. Similarly to the trivalent iron, the energy values of Fe(II) are not absolute, so the Fe(II) features were shifted to best match: 0.8 eV in IE and 1.4 eV in ET compared to the Fe(III). The shift in ET was larger than that in IE, which has been observed previously.[99,100]

The RIXS analyses performed for three Fe-BDC films, each deposited at different temperature, interestingly reveal the Fe(II) content to linearly increase with an increasing deposition temperature: the Fe(II) content was 5% for 250 °C, 18% for 280 °C, and 27% for 300 °C. Calculating the absolute values for the Fe(II) content however involves a considerable margin of error due to the significant Fe(III) and Fe(II) signal overlap. Thus, we utilized ^{57}Fe Mössbauer spectroscopy—a uniquely accurate tool for investigating local hyperfine interactions around iron atoms—to obtain definite values for the Fe(III) and Fe(II) contents in the Fe-BDC films.

Presence of the two different iron oxidation states was evident from the ^{57}Fe Mössbauer spectra as well [Figure 5 (f,g)]; for both deposition temperatures investigated, i.e., 250 and 300 °C, the component assigned to Fe(II) is clearly distinguished by its large isomer shift (blue line). In addition, two components (red and brown) typical of Fe(III) are visible in the spectra. The black quadruple doublet originates from traces of iron in the beryllium window of the detector. The isomer shift values (Table S1) are similar to the known mixed-valent bulk Fe-BDC materials.[101,102] The Fe(II) content (~32% for 250 °C and ~46% for 300 °C) was found higher than estimated from RIXS analysis. This is not surprising since the weaker Fe(II) RIXS signal was partly masked by the strong Fe(III) signal, which resulted in lower values than the actual Fe(II) content. A schematic summary shown in Figure 5(h) combines (i) the linear trend between the Fe(III)/Fe(II) ratio and the deposition temperature derived from the RIXS analyses and (ii) the expected definite Fe(III)/Fe(II) ratio at each temperature derived from the Mössbauer analysis.

The source for the divalent iron is unknown, but some partial reduction must take place during the deposition since initially only trivalent iron is present from the $FeCl_3$ precursor. For reported mixed-valent bulk Fe-BDC samples, the mixed valency has been achieved through the use of mixed precursors of $FeCl_3{\cdot}6H_2O$ and $FeCl_2{\cdot}4H_2O$ or through the hydrolysis of the typically used DMF solution.[43,101,102] For the ALD/MLD grown Fe-BDC thin films, the reduction of gaseous $FeCl_3$ to $FeCl_2$ is excluded as it is stable under the deposition conditions; it has been used frequently for the deposition of $Fe(III)_2O_3$ thin films under similar conditions (temperature), and even at 500 °C.[103−107] One possibility could be a reductive elimination which is a known reaction path both in ALD[108,109] and in organometallic systems in general, especially for the first-row transition metals. It also advocates a reaction mechanism pathway which does not effectively change the composition (creating new chemical species) of the films. For instance, the reduction could occur through Cl_2 elimination of chemisorbed $FeCl_xBDC_y$ moieties. Often the elimination of chlorine gas from metal−organic moieties is photodriven but thermal elimination is possible as well and driven by high temperatures and steric factors (bulky H_2BDC).[110,111] Another possibility for the reduction could in principle be a reductive elimination of the hypochlorite derivative of the terephthalate moiety, again driven by high deposition temperature and steric hindrance of the large organic linkers. These are however only speculative suggestions, and more in-depth analysis is required to clarify the true nature of the reduction mechanism.

3.4. Local Symmetry around Fe. In addition to the obtained oxidation states, relevant information about local bonding symmetry could be extracted from the Mössbauer spectra. The brown Fe(III) component is a singlet, indicative of a highly symmetric surrounding, while the red Fe(III) component has a small quadruple splitting, pointing toward a small distortion of the surroundings. Note that the ratio of the two Fe(III) components remains essentially unchanged with the increased deposition temperature, indicating that both trivalent Fe species get equally reduced. On the other hand, a relatively large quadruple splitting (i.e., distortion) can be observed for the Fe(II) component. However, it should be again noted that divalent iron generally has a larger splitting compared to trivalent iron due to its sixth 3*d* electron which breaks the spherical symmetry of the electron cloud, causing additional splitting even in rather symmetric surroundings. Hence the degree of distortion is somewhat difficult to determine for divalent Fe. Notably, the large and the small splitting of the Fe(II) and the red Fe(III) components, respectively, are in good agreement with the reported bulk Fe-BDC,[101,102] but the singlet Fe(III) has not been observed previously and hence indicates a somewhat different (local) structure for our Fe-BDC thin films.

The RIXS analysis suggests that a weak distortion of the iron octahedra may be possible, but due to the broadening of the RIXS features, it could not be unambiguously determined. The distortion would split the t_{2g} and e_g orbitals and thus split the RIXS features. The splitting was studied through calculations using D_{4h} (tetragonal distortion) which adds two parameters to the crystal field (Ds and Dt). At small values (−0.02 eV < (Ds, Dt) < 0.02 eV), i.e., when the distortion and thus the splitting is small, no real difference was seen due to the broadening of the experimental spectra. However, at higher (Ds, Dt) values, the calculated spectra looked clearly different from the experimental one. Hence within the parameter range used, the iron coordination seems octahedral, but a slight distortion cannot be ruled out.

3.5. Crystal Structure. First, the crystallinity of the ALD/MLD grown Fe-BDC thin films was screened over the entire deposition temperature range using in-house GIXRD. As visible in Figure 6(a), intensive diffractions at 0.72 Å^{-1} (d = 8.76 Å) and 0.74 Å^{-1} (d = 8.55 Å), highlighted with pink dashed lines and characteristic of long-range order, appear in the 240−250 °C deposition temperature range and disappear for the films deposited at 280 °C or higher. Therefore, we selected those two deposition temperatures (250 and 280 °C) for a more detailed characterization via synchrotron GIXRD. The use of a large-area detector allows one to collect wide-range reciprocal space maps (RSMs) in contrast to the 1D out-of-plane scans of the in-house GIXRD. The RSMs of Fe-BDC thin films deposited at 250 and 280 °C [Figure 6(b)] show the presence of incomplete Debye−Scherrer diffraction rings, thus denoting preferred crystalline orientation in the films. This explains the disappearance of the long-range order peaks in the in-house diffraction patterns for the 280 °C sample, as those are only present in the in-plane region (yellow guidelines). Despite differences in the degrees of orientation, the complete integration of the RSMs produces similar 1D patterns for both deposition temperatures.

https://doi.org/10.1021/acs.chemmater.4c00555
Chem. Mater. 2024, 36, 6489−6503

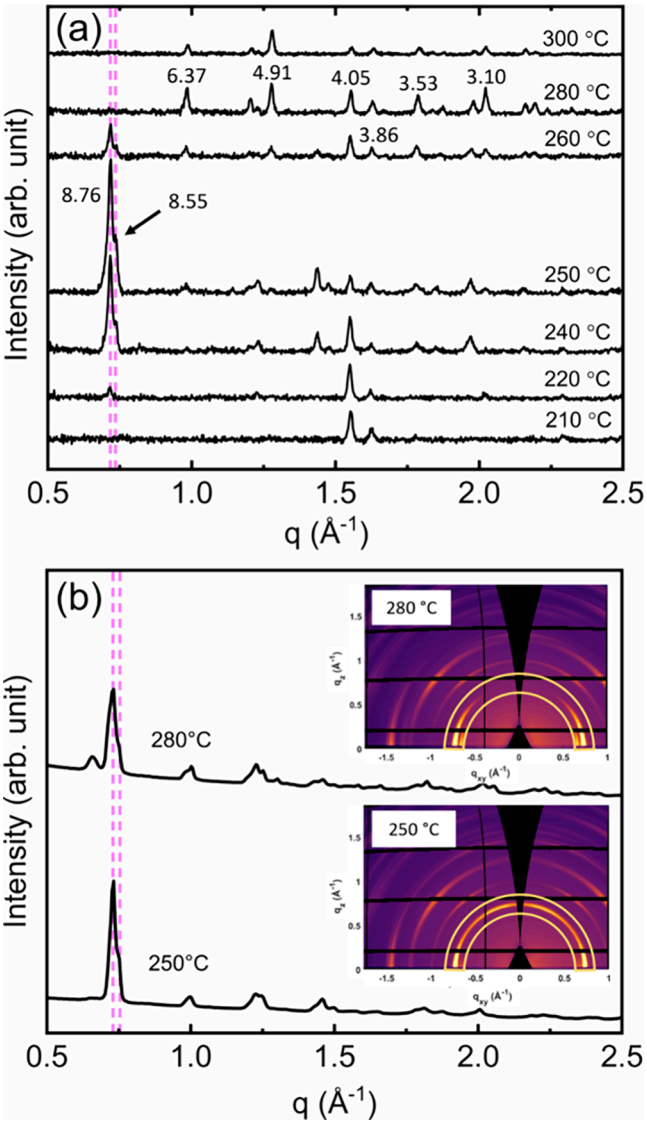

Figure 6. (a) In-house GIXRD and (b) synchrotron GIXRD patterns of Fe-BDC thin films at indicated deposition temperatures. RSMs of the synchrotron GIXRD measurements are inserted together with the corresponding diffractograms produced from the entire maps. The signals related to the orientation change in the diffractograms and the area where the long-range order peaks appear in the RMSs are highlighted with pink dashed and light-yellow lines, respectively. The *d*-values (Å) are shown for the main peaks in the in-house GIXRD pattern.

The measured GIXRD patterns do not match with any known crystal structure reported so far, though they somewhat resembles those of the MIL-53(Fe) and MOF-2 reported for other metal-BDC materials (Cu-BDC and Zn-BDC).[32,33,112] However, these materials cannot provide a proper match for the present Fe-BDC thin films as the MIL-53(Fe) contains guest moieties and the MOF-2 structures are based on purely divalent metal species. The reported Fe-BDC bulk samples with mixed valency (and again guest moieties) have different structures to our ALD/MLD grown films as well.[101,102]

Since no matching crystalline structures could be found in the literature, we carried out computational predictions for this unprecedented structure starting from a trivalent Fe(III)-BDC phase. An excellent candidate with the best match with the experimental data was obtained through optimizing the previously reported Sc(III)-BDC MOF structure[75] with Sc replaced by Fe. The predicted structure [monoclinic, space group *C*2/*c* (no. 15)] has 6-fold nearly symmetric octahedral Fe coordination which is in good agreement with the RIXS observations. Harmonic frequency calculations further confirmed the structure as a true local minimum. We also used this structure to calculate IR and Raman spectra (Figure S7), which correspond with the respective experimental spectra showing the expected features for the bond vibrations (bridging mode) discussed earlier. Additionally, the XRR-evaluated density of the thin films (~1.40 g/cm^3) is in good agreement with the predicted *C*2/*c* structure (DFT-PBE0) with the density calculated at 1.36 g/cm^3. Most notably, the predicted XRD pattern matches well with the experimental synchrotron GIXRD patterns (Figure 7).

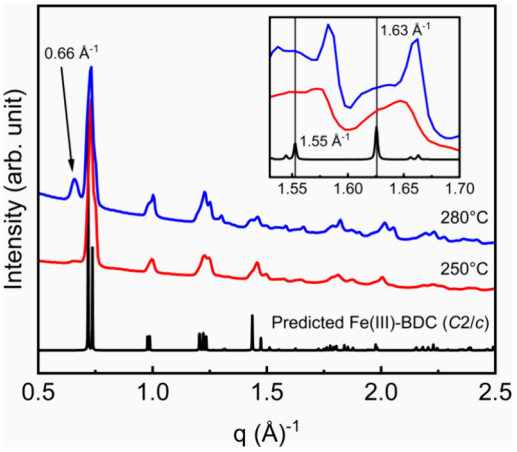

Figure 7. Synchrotron GIXRD patterns of Fe-BDC thin films deposited at indicated temperatures compared with the simulated pattern of the predicted Fe(III)-BDC *C*2/*c* structure. The unmatched (0.66 Å^{-1}) and the unexpectedly intense (1.55 and 1.63 Å^{-1}) diffractions are indicated with an arrow and in the inset, respectively. The intensities of the diffraction patterns

However, there are two main discrepancies. First, for the thin film deposited at 280 °C, the peak appearing at 0.66 Å^{-1} is not described by the predicted *C*2/*c* structure. We can only ascribe this to the appearance of a minor unidentified crystal phase at elevated deposition temperatures. Second, the diffraction peaks at 1.55 Å^{-1} (d = 4.05 Å) and 1.63 Å^{-1} (d = 3.86 Å), highlighted in the inset of Figure 7, have somewhat higher than expected intensities especially for the in-house GIXRD patterns (Figure S8), where these peaks have relatively high intensities already for the films deposited at 210−220 °C and then remain up to 300 °C. These diffractions could be attributed to the Fe(III)-BDC *C*2/*c* to 20$\bar{2}$ and $\bar{2}$21 reflections and their large intensities in in-house GIXRD to a strong out-of-plane orientation. Alternatively, they could also be caused by the presence of a minor unidentified crystal phase or a byproduct. Note that the small peak shift (inset) is ascribed to small deviations in the sample height and refraction effects at the air−film interface.[113]

To search for a possible minor Fe(III)-BDC phase, we used the USPEX/DFTB crystal structure prediction method. A trigonal Fe(III)-BDC crystal structure [space group *R*-3 (no. 148)] with similar structural motifs and 7 kJ/mol/*Z* lower in energy compared to the Sc-BDC based monoclinic *C*2/*c* structure was obtained. This structure was also confirmed as a

https://doi.org/10.1021/acs.chemmater.4c00555
Chem. Mater. 2024, 36, 6489−6503

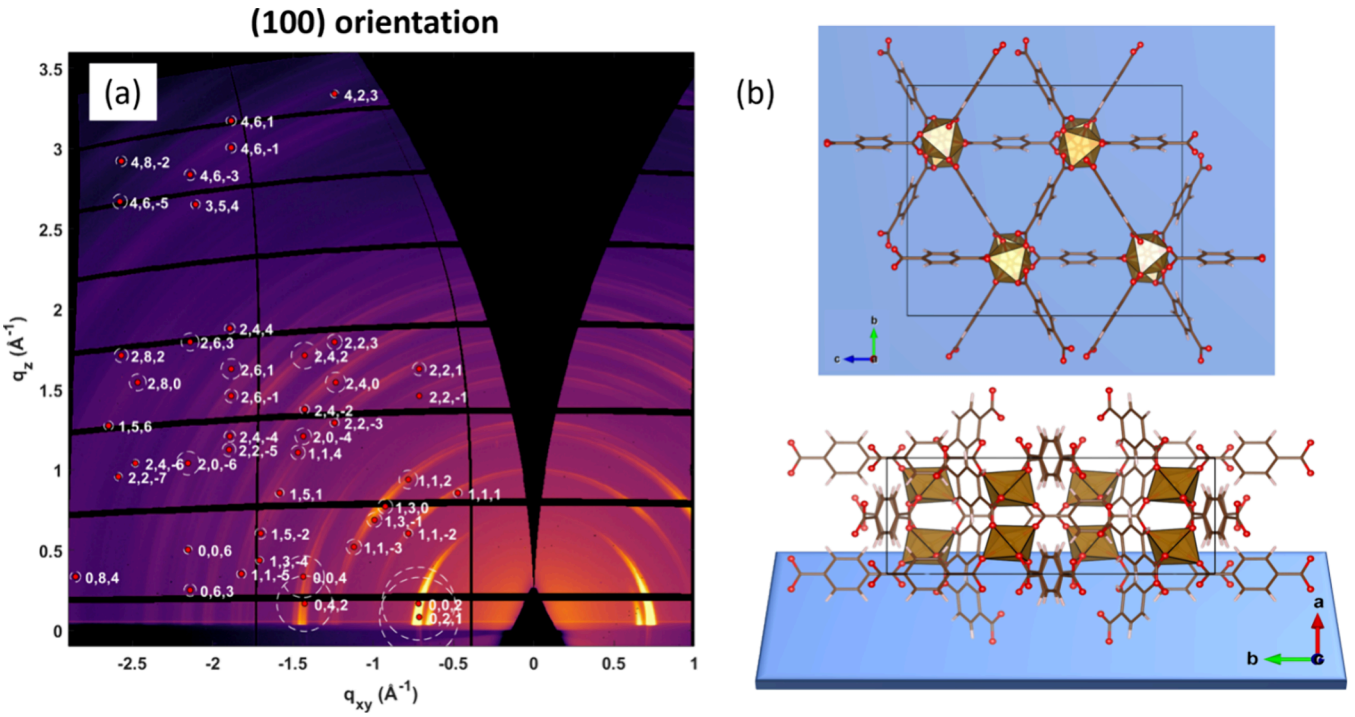

Figure 8. (a) RSM of a Fe-BDC thin film deposited at 280 °C obtained from synchrotron GIXRD. The simulated Bragg peaks for a (100) crystalline orientation are overlaid on the negative q_{xy} side of the map. Red points at the center of circles give the expected positions of the Bragg peaks, and the areas inside the circles give the square of the structure factors, which are proportional to the expected intensities. (b) Schematic illustration of the *C*2/*c* structure drawn with VESTA[114] in the preferred orientation (the triangular channels laying perpendicular) with respect to the substrate (top and side view). The BDC backbone is drawn in stick style, the red balls are oxygen, and the Fe atoms locate inside the brown octahedra.

true local minimum with harmonic frequency calculations when reoptimized with CRYSTAL. When considered per atom, the energy difference between these two crystal structures is only 0.15 kJ/mol/atom, making both energetically feasible. Furthermore, investigation of Gibbs free energy within the harmonic approximation shows that the Sc-BDC based *C*2/*c* structure becomes thermodynamically favorable compared to the USPEX-predicted *R*-3 one above 350 K, with the difference at 300 K being already negligible (0.02 kJ/mol/atom). However, the simulated diffractogram of the USPEX-predicted *R*-3 structure does not match with either the 0.66, 1.55, or 1.63 Å^{-1} peaks (Figure S9) and thus cannot represent any existing minority phase.

The existence of a secondary Fe(II)-BDC crystal phase could also explain these unmatched diffractions. Hence, we resorted to computational modeling to generate possible Fe(II)-BDC crystal structures both via the USPEX/DFTB crystal structure prediction runs and reoptimizing known divalent MOF-2 (Cu)[76] and MOF-71 (Co)[77] structures. The lowest-energy Fe(II)-BDC structure from the USPEX runs has a monoclinic symmetry [space group $P2_1/c$ (no. 14)] with a 4-fold Fe coordination. Another high-symmetry structure with tetragonal symmetry [space group $I4_1$ (no. 80)] was found to also have reasonable energetics and 4-fold coordination which contradicts with the experimental (RIXS) results. For the reoptimized MOFs, the Fe(II) MOF-2 based structure has the space group *P*-1 (no. 2) and 55 kJ/mol/Z lower energy compared to the lowest-energy USPEX structure. The Fe(II) MOF-71 based structure adopts the space group *C*2 (no. 5) which is energetically closer to the USPEX-predicted structures but still 9 kJ/mol/Z more favorable compared to them. Runs with the USPEX algorithm incorporating both Fe(III) and Fe(II) were performed as well but they did not yield reasonable high-symmetry structures, with all of the lowest-energy structures having the space group *P*1 (no. 1). In these structures, Fe had 4-fold, 5-fold, and 6-fold coordination. The experimentally known MOF-2 (for Cu)[76] and MOF-71 (for Co)[77] structures were found to be energetically more favorable compared to any of the Fe(II)-based structures produced by USPEX. This indicates that for compositions with Fe(II) the algorithm was not as efficient in predicting low energy structures as for Fe(III). Furthermore, same as for the USPEX-derived Fe(III)-BDC structure, neither of the MOF-derived nor the USPEX-derived Fe(II)-BDC structures could fully explain the additional 0.66, 1.55, or 1.63 Å^{-1} peaks (Figure S9). Therefore, we attribute the significant Fe(II) content in the films described above to a largely amorphous Fe(II)-BDC phase. We reason that, for such a significant Fe(II) presence (from ∼32% at 250 °C to ∼46% at 300 °C), a crystalline material would generate a more intense diffraction from a larger number of unmatched reflections.

To investigate the crystalline orientation of the films, we plotted the simulated Bragg peaks of the best predicted Fe(III)-BDC *C*2/*c* structure overlaid with the RSMs and analyzed for possible orientations. As visible in Figure 8(a), for a Fe-BDC film deposited at 280 °C, the (100) orientation yields the best matching, but contributions from other ones cannot be discarded (Figure S10). For the 250 °C sample, the (011) and (012) orientations could explain the appearance of higher intensity 002 and 021 reflections at higher q_z values. These disappear for the 280 °C thin film, which denotes an evolution to a more dominant film texture. Also, another

https://doi.org/10.1021/acs.chemmater.4c00555
Chem. Mater. 2024, 36, 6489−6503

explanation for the unexpected high intensity of the 1.58 and 1.66 Å^{-1} peaks could come from a mixture of $(10\bar{1})$ and $(\bar{2}21)$ orientations (Figure S10). The (100), $(10\bar{1})$, and $(\bar{2}21)$ orientations all correspond to the triangular channels of the crystal structure laying approximately perpendicular to the substrate [Figure 8(b)].

3.6. Concluding Remarks on Structure and Composition. Both the RIXS and Mössbauer analyses indicated that our ALD/MLD-grown Fe-BDC thin films contain both Fe(III) and Fe(II) species. For the former, the computationally predicted monoclinic Fe(III)-BDC *C*2/*c* structure could be established, while, for the latter, no reasonable Fe(II)-BDC crystal structure model could be predicted or experimentally discerned. Thus, some uncertainty on both the structure and composition of the Fe(II)-containing phase remain.

While the Fe(II)-based structure could not be unambiguously addressed, exploring the fine details of the Mössbauer spectra provided some useful information on the local structure of the Fe(II) species. In general, narrow and broad Mössbauer line widths are expected for crystalline and amorphous materials, respectively. Somewhat contradictory to our conjecture of the amorphous Fe(II)-BDC phase, the Fe(II) component in the present Fe-BDC Mössbauer spectra has a very narrow line width. To confirm this, we refitted the spectra shown in Figure 5 with nonfixed line widths for the different Fe components and found the Fe(II) to have even narrower line width (0.221−0.237 mm/s) than the Fe(III) components (0.329−0.368 mm/s). This could suggest a crystalline phase also for Fe(II) but does not exclude the possibility of an amorphous Fe(II) phase either; the Fe(II) species in an amorphous surrounding can have even greater local order compared to crystalline phase due to relaxation of bonds. Regarding the Fe(III) phase, the predicted *C*2/*c* structure has only one type of Fe(III) octahedra in the structure and it is slightly distorted (Table S2). The degree of the distortion matches with the slightly split Fe(III) component in the Mössbauer spectra. This was evaluated using point-charge calculation of the electric-field gradient acting on the ^{57}Fe nucleus (as the high-spin trivalent state was regarded as highly probable, no *d*-electron contributions were considered). However, there is also a peculiarity related to the Fe(III)-BDC phase, as the source of the singlet Fe(III) component seen in the Mössbauer spectra remains inconclusive. Possibly, the real Fe(III)-BDC structure is partly composed of more symmetric octahedra than the predicted *C*2/*c* structure suggests.

The other relevant question to be addressed is the chemical composition of the Fe(II)-containing phase, in other words, whether the Fe(II) species are bonded to BDC ligands or some other counterions. While we do not have definitive evidence of the existence of the Fe(II)-BDC phase (as, e.g., FTIR does not unambiguously distinguish Fe(II)-BDC from Fe(III)-BDC), we would like to emphasize that there are no indications of any other Fe(II)-containing material either. Since the deposition process involves the use of only two stable chemical precursors, no other Fe-based materials should form in such high quantities. For example, formation of inorganic decomposition products such as Fe(II) oxides, carbides, or carbonates would require an unlikely dissociation/reduction of the stable COO^- group (the only oxygen source present) and/or decomposition of the stable BDC backbone. Moreover, these decomposition products would result in different experimental results (GPC, film density, IR/Raman spectra, Mössbauer spectra) from the observed ones. To conclude, no other significant material phases than Fe(III)-BDC and Fe(II)-BDC can be expected to be present in the films.

3.7. Film Stability. From a practical point of view, film stability is one of the main concerns for metal−organic thin films. Hence, we investigated the thermal stability of the films by performing in situ FTIR measurements at gradually elevated temperatures (40−600 °C). The measurements were done both in inert (N_2) atmosphere and in air. Remarkably, the Fe-BDC thin films were stable up to 400 °C in N_2 atmosphere and 300 °C in air, as there were no signs of chemical degradation according to in situ FTIR measurements (Figure 9). Once

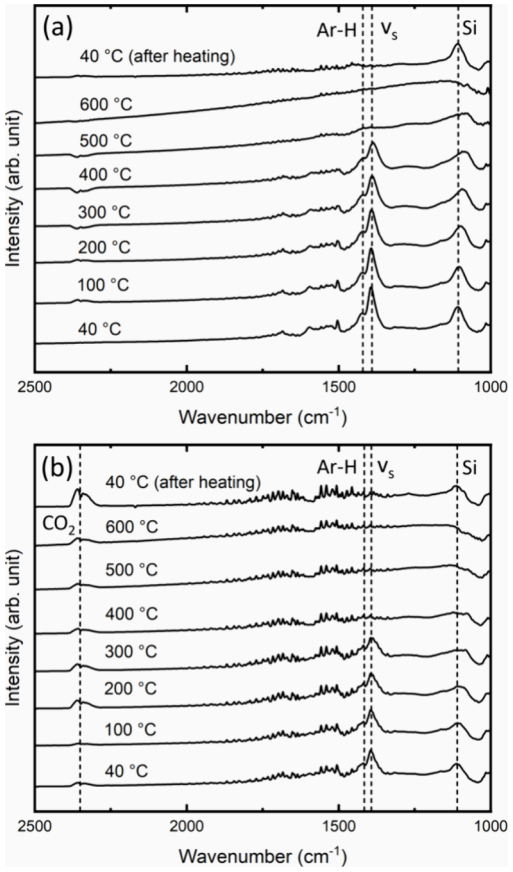

Figure 9. In-situ FTIR spectra for Fe-BDC thin films measured at elevated temperatures (a) under N_2 flow and (b) in a sealed compartment in air. The temperature was kept at each given temperature for 20 min before measuring the corresponding spectrum.

annealed in N_2 at 500 °C or in air at 400 °C, the features related to Fe−OCO−Fe bonding and aromatic ring stretch vibrations vanished, indicating a total decomposition of the films and evaporation of the organic decomposition products. Figure S11 shows more precisely that no significant changes were observed while keeping the samples at 400 °C (N_2) and 300 °C (air) for 20 min, but obvious decomposition was observed at 500 °C (N_2) and 400 °C (air) during the 20 min waiting time. The stability of the Fe-BDC films is similar or even better than the bulk counterparts for which the decomposition temperature is in the range of 300−500 °C in inert conditions.[115−117]

We validated the results by also studying the effect of elevated temperatures in air on film thickness [Figure S12(a)]

https://doi.org/10.1021/acs.chemmater.4c00555
Chem. Mater. 2024, 36, 6489−6503

by heating the sample in a regular open furnace and performing the measurements in between different temperatures. No significant changes were observed in film thickness until the decomposition temperature estimated from the in situ experiments, at which the thickness decreased to nearly zero. The room-temperature FTIR spectra for the samples heated in the open furnace were also recorded and are shown in Figure S12(b). After heating at 350 °C, all the IR signals related to the Fe-BDC material had vanished and only peaks related to remaining Fe−O/Fe−OH[118] species could be seen. These results confirm the excellent thermal stability of the Fe-BDC films both in inert and oxidative conditions well above the deposition temperatures. Note that this also confirms our earlier conclusion that the reduction of Fe(III) is not caused by film decomposition.

4. CONCLUSIONS

We have implemented an extensive combination of experimental and computational methods to study the composition and structure of highly stable Fe-BDC thin films grown via the robust, industry-feasible gas-phase ALD/MLD technique at 210−300 °C. FTIR and Raman measurements showed the anticipated chemical composition (−Fe−OCO−C_6H_4−OCO−Fe−) and a bridging type bonding scheme. The RIXS and ^{57}Fe Mössbauer analyses revealed the existence of both octahedral Fe(III) and Fe(II) in the films, and the portion of Fe(II) was found to increase with increasing deposition temperature. The mechanism for this partial reduction remained unclear, but the decomposition of the Fe(III)Cl_3 precursor was ruled out and a reductive elimination reaction was tentatively suggested. Most excitingly, we found a highly feasible, novel monoclinic crystal structure candidate for the Fe(III)-BDC phase (space group $C2/c$) by means of combining synchrotron GIXRD analysis and crystal structure prediction through optimizing a previously reported Sc(III)-BDC crystal structure. For the Fe(II)-BDC phase, crystal structure predictions did not yield any conclusive results and we believe that divalent iron in the films exists in an amorphous form.

This work provides a valuable example of how novel chemical and structural features can be resolved even for previously unknown thin film materials with no equivalent bulk material available for comparison or a possibility to utilize traditional characterization techniques such as Rietveld refinement. Moreover, to respond to the great need of advanced deposition methods, these results emphasize the role of ALD/MLD as a pivotal solvent-free technique for the growth of even otherwise inaccessible hybrid materials via industry feasible thin-film deposition routes.

■ ASSOCIATED CONTENT

Supporting Information

The Supporting Information is available free of charge at https://pubs.acs.org/doi/10.1021/acs.chemmater.4c00555.

Additional experimental materials of film thickness, density, and roughness (XRR), morphology (SEM, AFM), and composition (FTIR), local environments of Fe (RIXS), hyperfine parameters of Fe (^{57}Fe Mössbauer), crystal structure comparison and texture (IR, Raman, GIXRD, RSMs), bond lengths and angles of Fe octahedra, film stability (XRR, FTIR), and additional computational details including USPEX simulation runs, Monkhorst−Pack k-meshes used for the different Fe-BDC structures, and optimized crystal structures in CIF format (PDF)

■ AUTHOR INFORMATION

Corresponding Author

Maarit Karppinen − *Department of Chemistry and Materials Science, Aalto University, FI-00076 Aalto, Finland;* orcid.org/0000-0003-1091-1169; Email: maarit.karppinen@aalto.fi

Authors

Topias Jussila − *Department of Chemistry and Materials Science, Aalto University, FI-00076 Aalto, Finland;* orcid.org/0000-0002-0435-0660

Anish Philip − *Department of Chemistry and Materials Science, Aalto University, FI-00076 Aalto, Finland;* orcid.org/0000-0001-9978-210X

Víctor Rubio-Giménez − *Centre for Membrane Separations, Adsorption, Catalysis and Spectroscopy (cMACS), Katholieke Universiteit Leuven, 3001 Leuven, Belgium;* orcid.org/0000-0003-1269-5885

Kim Eklund − *Department of Chemistry and Materials Science, Aalto University, FI-00076 Aalto, Finland*

Sami Vasala − *ESRF - The European Synchrotron, 38000 Grenoble, France*

Pieter Glatzel − *ESRF - The European Synchrotron, 38000 Grenoble, France*

Johan Lindén − *Physics/Faculty of Science and Engineering, Åbo Akademi University, FI-20500 Turku, Finland*

Teruki Motohashi − *Department of Applied Chemistry, Kanagawa University, Yokohama 221-8686, Japan;* orcid.org/0000-0002-4568-5600

Antti J. Karttunen − *Department of Chemistry and Materials Science, Aalto University, FI-00076 Aalto, Finland;* orcid.org/0000-0003-4187-5447

Rob Ameloot − *Centre for Membrane Separations, Adsorption, Catalysis and Spectroscopy (cMACS), Katholieke Universiteit Leuven, 3001 Leuven, Belgium;* orcid.org/0000-0003-3178-5480

Complete contact information is available at: https://pubs.acs.org/10.1021/acs.chemmater.4c00555

Author Contributions

The manuscript was written through contributions of all authors. All authors have given approval to the final version of the manuscript.

Notes

The authors declare no competing financial interest.

■ ACKNOWLEDGMENTS

Funding was received from the European Union (ERC AdG, UniEnMLD, No. 101097815). Views and opinions expressed are however those of the authors only and do not necessarily reflect those of the European Union or the European Research Council. Neither the European Union nor the granting authority can be held responsible for them. This work was also partly supported by the Finnish Cultural Foundation (THERMOF), Magnus Ehrnrooth Foundation, KU Leuven (GSFAH/22/001), Research Foundation Flanders (1263622N), JSPS KAKENHI (JP22H05143; Transformative Research Areas (A) "Supra-ceramics"), and Scandinavia-Japan

Sasakawa Foundation. We acknowledge the European Synchrotron Radiation Facility (ESRF) for provision of synchrotron radiation facilities (beamline ID26) under the proposal number CH-6525 (DOI: 10.15151/ESRF-ES-894388406). We also acknowledge Diamond Light Source for time on Beamline I07 under proposal si29967 and thank Francesco Carlà, Jonathan Rawle, Jorid Smets, and Jesús Gándara-Loe. We also thank CSC − the Finnish IT Center for Science for computational resources. Anni Virta and Mikhail Kuklin are acknowledged for contributions to the USPEX crystal structure predictions. Olga Partanen is acknowledged for contributions to the thermal stability studies. Miwa Saito and Yusuke Asai are acknowledged for contributions to the in situ FTIR experiments.

REFERENCES

(1) Cheetham, A. K.; Rao, C. N. R.; Feller, R. K. Structural diversity and chemical trends in hybrid inorganic−organic framework materials. *Chem. Commun.* **2006**, 4780−4795.
(2) Gagliardi, L.; Yaghi, O. M. Three Future Directions for Metal−Organic Frameworks. *Chem. Mater.* **2023**, *35*, 5711−5712.
(3) Stassen, I.; Burtch, N.; Talin, A.; Falcaro, P.; Allendorf, M.; Ameloot, R. An updated roadmap for the integration of metal−organic frameworks with electronic devices and chemical sensors. *Chem. Soc. Rev.* **2017**, *46*, 3185−3241.
(4) Crivello, C.; Sevim, S.; Graniel, O.; Franco, C.; Pané, S.; Puigmartí-Luis, J.; Muñoz-Rojas, D. Advanced technologies for the fabrication of MOF thin films. *Mater. Horiz.* **2021**, *8*, 168−178.
(5) Multia, J.; Karppinen, M. Atomic/molecular layer deposition for designer's functional metal−organic materials. *Adv. Mater. Interfaces* **2022**, *9*, No. 2200210.
(6) Zhao, Y.; Zhang, L.; Liu, J.; Adair, K.; Zhao, F.; Sun, Y.; Wu, T.; Bi, X.; Amine, K.; Lu, J.; Sun, X. Atomic/molecular layer deposition for energy storage and conversion. *Chem. Soc. Rev.* **2021**, *50*, 3889−3956.
(7) George, S. M. Atomic layer deposition: an overview. *Chem. Rev.* **2010**, *110*, 111−131.
(8) Bergsman, D. S.; Closser, R. G.; Bent, S. F. Mechanistic Studies of Chain Termination and Monomer Absorption in Molecular Layer Deposition. *Chem. Mater.* **2018**, *30*, 5087−5097.
(9) Philip, A.; Niemelä, J.-P.; Tewari, G. C.; Putz, B.; Edwards, T. E. J.; Itoh, M.; Utke, I.; Karppinen, M. Flexible ε-Fe2O3-terephthalate thin-film magnets through ALD/MLD. *ACS Appl. Mater. Interfaces* **2020**, *12*, 21912−21921.
(10) Philip, A.; Zhou, Y.; Tewari, G. C.; van Dijken, S.; Karppinen, M. Optically controlled large-coercivity room-temperature thin-film magnets. *J. Mater. Chem. C* **2021**, *10*, 294−300.
(11) Kao, C.-Y.; Li, B.; Lu, Y.; Yoo, J.-W.; Epstein, A. J. Thin films of organic-based magnetic materials of vanadium and cobalt tetracyanoethylene by molecular layer deposition. *J. Mater. Chem. C* **2014**, *2*, 6171−6176.
(12) Ghazy, A.; Ylönen, J.; Subramaniyam, N.; Karppinen, M. Atomic/molecular layer deposition of europium−organic thin films on nanoplasmonic structures towards FRET-based applications. *Nanoscale* **2023**, *15*, 15865−15870.
(13) Ghazy, A.; Lastusaari, M.; Karppinen, M. Excitation Wavelength Engineering through Organic Linker Choice in Luminescent Atomic/Molecular Layer Deposited Lanthanide−Organic Thin Films. *Chem. Mater.* **2023**, *35*, 5988−5995.
(14) Silva, R. M.; Carlos, L. D.; Rocha, J.; Silva, R. F. Luminescent thin films of Eu-bearing UiO-66 metal organic framework prepared by ALD/MLD. *Appl. Surf. Sci.* **2020**, *527*, No. 146603.
(15) Hansen, P.-A.; Holm Sørensen, S.; Desbois, N.; Gros, C. P.; Nilsen, O. Perylenes, Porphyrins, and Other Large Dye Molecules for Molecular Layer Deposition. *Adv. Mater. Interfaces* **2024**, *11*, No. 2300667.
(16) Marin, G.; Funahashi, R.; Karppinen, M. Textile-Integrated ZnO-Based Thermoelectric Device Using Atomic Layer Deposition. *Adv. Eng. Mater.* **2020**, *22*, No. 2000535.
(17) Krahl, F.; Giri, A.; Tomko, J. A.; Tynell, T.; Hopkins, P. E.; Karppinen, M. Thermal conductivity reduction at inorganic−organic interfaces: from regular superlattices to irregular gradient layer sequences. *Adv. Mater. Interfaces* **2018**, *5*, No. 1701692.
(18) Philip, A.; Ghiyasi, R.; Karppinen, M. Visible-light absorbing TiO2: curcumin thin films with ALD/MLD. *ChemNanoMat* **2021**, *7*, 253−256.
(19) Momtazi, L.; Sønsteby, H. H.; Dartt, D. A.; Eidet, J. R.; Nilsen, O. Bioactive titaminates from molecular layer deposition. *RSC Adv.* **2017**, *7*, 20900−20907.
(20) Nisula, M.; Karppinen, M. In situ lithiated quinone cathode for ALD/MLD-fabricated high-power thin-film battery. *J. Mater. Chem. A* **2018**, *6*, 7027−7033.
(21) Kazyak, E.; Shin, M.; LePage, W. S.; Cho, T. H.; Dasgupta, N. P. Molecular layer deposition of Li-ion conducting "Lithicone" solid electrolytes. *Chem. Commun.* **2020**, *56*, 15537−15540.
(22) Van de Kerckhove, K.; Mattelaer, F.; Dendooven, J.; Detavernier, C. Molecular layer deposition of "vanadicone", a vanadium-based hybrid material, as an electrode for lithium-ion batteries. *Dalton Trans.* **2017**, *46*, 4542−4553.
(23) Vandenbroucke, S. S. T.; Henderick, L.; De Taeye, L. L.; Li, J.; Jans, K.; Vereecken, P. M.; Dendooven, J.; Detavernier, C. Titanium Carboxylate Molecular Layer Deposited Hybrid Films as Protective Coatings for Lithium-Ion Batteries. *ACS Appl. Mater. Interfaces* **2022**, *14*, 24908−24918.
(24) Bergsman, D. S.; Baker, J. G.; Closser, R. G.; MacIsaac, C.; Lillethorup, M.; Strickler, A. L.; Azarnouche, L.; Godet, L.; Bent, S. F. Structurally Stable Manganese Alkoxide Films Grown by Hybrid Molecular Layer Deposition for Electrochemical Applications. *Adv. Funct. Mater.* **2019**, *29*, No. 1904129.
(25) Multia, J.; Heiska, J.; Khayyami, A.; Karppinen, M. Electrochemically Active In Situ Crystalline Lithium-Organic Thin Films by ALD/MLD. *ACS Appl. Mater. Interfaces* **2020**, *12*, 41557−41566.
(26) Kint, J.; Mattelaer, F.; Vandenbroucke, S. S. T.; Muriqi, A.; Minjauw, M. M.; Nisula, M.; Vereecken, P. M.; Nolan, M.; Dendooven, J.; Detavernier, C. Molecular Layer Deposition of "Magnesicone", a Magnesium-based Hybrid Material. *Chem. Mater.* **2020**, *32*, 4451−4466.
(27) Chen, Z.; Wang, H.; Wang, X.; Chen, P.; Liu, Y.; Zhao, H.; Zhao, Y.; Duan, Y. Low-temperature remote plasma enhanced atomic layer deposition of ZrO2/zircone nanolaminate film for efficient encapsulation of flexible organic light-emitting diodes. *Sci. Rep.* **2017**, *7*, 40061.
(28) Chen, G.; Weng, Y.; Sun, F.; Zhou, X.; Wu, C.; Yan, Q.; Guo, T.; Zhang, Y. Low-temperature atomic layer deposition of Al2O3/alucone nanolaminates for OLED encapsulation. *RSC Adv.* **2019**, *9*, 20884−20891.
(29) Khayyami, A.; Philip, A.; Karppinen, M. Atomic/molecular layer deposited iron−azobenzene framework thin films for stimuli-induced gas molecule capture/release. *Angew. Chem., Int. Ed.* **2019**, *58*, 13400−13404.
(30) Safdar, M.; Ghazy, A.; Tuomisto, M.; Lastusaari, M.; Karppinen, M. Effect of carbon backbone on luminescence properties of Eu-organic hybrid thin films prepared by ALD/MLD. *J. Mater. Sci.* **2021**, *56*, 12634−12642.
(31) Momtazi, L.; Sønsteby, H. H.; Nilsen, O. Biocompatible organic−inorganic hybrid materials based on nucleobases and titanium developed by molecular layer deposition. *Beilstein J. Nanotechnol.* **2019**, *10*, 399−411.
(32) Ahvenniemi, E.; Karppinen, M. Atomic/molecular layer deposition: a direct gas-phase route to crystalline metal−organic framework thin films. *Chem. Commun.* **2016**, *52*, 1139−1142.
(33) Multia, J.; Kravchenko, D. E.; Rubio-Giménez, V.; Philip, A.; Ameloot, R.; Karppinen, M. Nanoporous Metal−Organic Framework Thin Films Prepared Directly from Gaseous Precursors by Atomic

https://doi.org/10.1021/acs.chemmater.4c00555
Chem. Mater. 2024, 36, 6489−6503

and Molecular Layer Deposition: Implications for Microelectronics. *ACS Appl. Nano Mater.* **2023**, *6*, 827−831.
(34) Gikonyo, B.; Liu, F.; De, S.; Journet, C.; Marichy, C.; Fateeva, A. Investigating the vapour phase synthesis of copper terephthalate metal organic framework thin films by atomic/molecular layer deposition. *Dalton Trans.* **2022**, *52*, 211−217.
(35) Nisula, M.; Karppinen, M. Atomic/Molecular Layer Deposition of Lithium Terephthalate Thin Films as High Rate Capability Li-Ion Battery Anodes. *Nano Lett.* **2016**, *16*, 1276−1281.
(36) Ahvenniemi, E.; Karppinen, M. In Situ Atomic/Molecular Layer-by-Layer Deposition of Inorganic−Organic Coordination Network Thin Films from Gaseous Precursors. *Chem. Mater.* **2016**, *28*, 6260−6265.
(37) Smets, J.; Cruz, A. J.; Rubio-Giménez, V.; Tietze, M. L.; Kravchenko, D. E.; Arnauts, G.; Matavž, A.; Wauteraerts, N.; Tu, M.; Marcoen, K.; et al. Molecular Layer Deposition of Zeolitic Imidazolate Framework-8 Films. *Chem. Mater.* **2023**, *35*, 1684−1690.
(38) Heiska, J.; Sorsa, O.; Kallio, T.; Karppinen, M. Benzenedisulfonic Acid as an ALD/MLD Building Block for Crystalline Metal-Organic Thin Films. *Chem. Eur. J.* **2021**, *27*, 8799−8803.
(39) Legenstein, L.; Rodríguez-Hermida, S.; Rubio-Giménez, V.; Stassin, T.; Hofer, S.; Kainz, M. P.; Fratschko, M.; Carraro, F.; Falcaro, P.; Ameloot, R.; Resel, R. Identifying the Internal Network Structure of a New Copper Isonicotinate Thin-Film Polymorph Obtained via Chemical Vapor Deposition. *Adv. Mater. Interfaces* **2023**, *10*, No. 2202461.
(40) Penttinen, J.; Nisula, M.; Karppinen, M. Atomic/Molecular Layer Deposition of s-Block Metal Carboxylate Coordination Network Thin Films. *Chem. Eur. J.* **2017**, *23*, 18225−18231.
(41) Nisula, M.; Linnera, J.; Karttunen, A. J.; Karppinen, M. Lithium Aryloxide Thin Films with Guest-Induced Structural Transformation by ALD/MLD. *Chem. Eur. J.* **2017**, *23*, 2988−2992.
(42) Tanskanen, A.; Karppinen, M. Iron-terephthalate coordination network thin films through in-situ atomic/molecular layer deposition. *Sci. Rep.* **2018**, *8*, 8976.
(43) Bara, D.; Meekel, E. G.; Pakamorė, I.; Wilson, C.; Ling, S.; Forgan, R. S. Exploring and expanding the Fe-terephthalate metal−organic framework phase space by coordination and oxidation modulation. *Mater. Horiz.* **2021**, *8*, 3377−3386.
(44) Gao, Y.; Li, S.; Li, Y.; Yao, L.; Zhang, H. Accelerated photocatalytic degradation of organic pollutant over metal-organic framework MIL-53(Fe) under visible LED light mediated by persulfate. *Appl. Catal. B: Environ.* **2017**, *202*, 165−174.
(45) Liang, R.; Jing, F.; Shen, L.; Qin, N.; Wu, L. MIL-53(Fe) as a highly efficient bifunctional photocatalyst for the simultaneous reduction of Cr(VI) and oxidation of dyes. *J. Hazard. Mater.* **2015**, *287*, 364−372.
(46) Ai, L.; Zhang, C.; Li, L.; Jiang, J. Iron terephthalate metal−organic framework: Revealing the effective activation of hydrogen peroxide for the degradation of organic dye under visible light irradiation. *Appl. Catal. B: Environ.* **2014**, *148*−*149*, 191−200.
(47) Ai, L.; Li, L.; Zhang, C.; Fu, J.; Jiang, J. MIL-53(Fe): A Metal−Organic Framework with Intrinsic Peroxidase-Like Catalytic Activity for Colorimetric Biosensing. *Chem. Eur. J.* **2013**, *19*, 15105−15108.
(48) Liang, L.; Huang, Y.; Liu, W.; Zuo, W.; Ye, F.; Zhao, S. Colorimetric Detection of Salicylic Acid in Aspirin Using MIL-53(Fe) Nanozyme. *Front. Chem.* **2020**, *8*, 671.
(49) Jiang, Y.; Yang, Q.-M.; Xu, Q.-J.; Lu, S.-Y.; Hu, L.-Y.; Xu, M.-W.; Liu, Y.-S. Metal organic framework MIL-53(Fe) as an efficient artificial oxidase for colorimetric detection of cellular biothiols. *Anal. Biochem.* **2019**, *577*, 82−88.
(50) Lu, J.; Xiong, Y.; Liao, C.; Ye, F. Colorimetric detection of uric acid in human urine and serum based on peroxidase mimetic activity of MIL-53(Fe). *Anal. Methods* **2015**, *7*, 9894−9899.
(51) Guillen, S. G.; Parres-Gold, J.; Ruiz, A.; Lucsik, E.; Dao, B.; Hang, T. K. L.; Chang, M.; Garcia, A. O.; Wang, Y.; Tian, F. pH-Responsive Metal−Organic Framework Thin Film for Drug Delivery. *Langmuir* **2022**, *38*, 16014−16023.
(52) Bui, A.; Guillen, S. G.; Sua, A.; Nguyen, T. C.; Ruiz, A.; Carachure, L.; Weber, M. D. R.; Cortez, A.; Tian, F. Iron-containing metal-organic framework thin film as a drug delivery system. *Colloids Surf. A: Physicochem. Eng.* **2022**, *650*, No. 129611.
(53) Mahdipoor, H. R.; Halladj, R.; Ganji Babakhani, E.; Amjad-Iranagh, S.; Sadeghzadeh Ahari, J. Synthesis, characterization, and CO2 adsorption properties of metal organic framework Fe-BDC. *RSC Adv.* **2021**, *11*, 5192−5203.
(54) Jin, Y.; Zhao, C.; Sun, Z.; Lin, Y.; Chen, L.; Wang, D.; Shen, C. Facile synthesis of Fe-MOF/RGO and its application as a high performance anode in lithium-ion batteries. *RSC Adv.* **2016**, *6*, 30763−30768.
(55) Hu, Z.; Tao, C.-a.; Liu, H.; Zou, X.; Zhu, H.; Wang, J. Fabrication of an NH2-MIL-88B photonic film for naked-eye sensing of organic vapors. *J. Mater. Chem. A* **2014**, *2*, 14222−14227.
(56) Li, M.; Zheng, Z.; Zheng, Y.; Cui, C.; Li, C.; Li, Z. Controlled Growth of Metal−Organic Framework on Upconversion Nanocrystals for NIR-Enhanced Photocatalysis. *ACS Appl. Mater. Interfaces* **2017**, *9*, 2899−2905.
(57) Scherb, C.; Schödel, A.; Bein, T. Directing the Structure of Metal−Organic Frameworks by Oriented Surface Growth on an Organic Monolayer. *Angew. Chem., Int. Ed.* **2008**, *47*, 5777−5779.
(58) Claes, B.; Boudewijns, T.; Muchez, L.; Hooyberghs, G.; Van der Eycken, E. V.; Vanderleyden, J.; Steenackers, H. P.; De Vos, D. E. Smart Metal−Organic Framework Coatings: Triggered Antibiofilm Compound Release. *ACS Appl. Mater. Interfaces* **2017**, *9*, 4440−4449.
(59) Dong, Y.-J.; Liao, J.-F.; Kong, Z.-C.; Xu, Y.-F.; Chen, Z.-J.; Chen, H.-Y.; Kuang, D.-B.; Fenske, D.; Su, C.-Y. Conformal coating of ultrathin metal-organic framework on semiconductor electrode for boosted photoelectrochemical water oxidation. *Appl. Catal. B: Environ.* **2018**, *237*, 9−17.
(60) Silva, R. M.; Rocha, J.; Silva, R. F. ALD/MLD coating of patterned vertically aligned carbon nanotube micropillars with Fe-NH2TP hybrids. *Nanoscale* **2023**, *15*, 10423−10429.
(61) Schrode, B.; Pachmajer, S.; Dohr, M.; Röthel, C.; Domke, J.; Fritz, T.; Resel, R.; Werzer, O. GIDVis: a comprehensive software tool for geometry-independent grazing-incidence X-ray diffraction data analysis and pole-figure calculations. *J. Appl. Crystallogr.* **2019**, *52*, 683−689.
(62) Glatzel, P.; Harris, A.; Marion, P.; Sikora, M.; Weng, T. C.; Guilloud, C.; Lafuerza, S.; Rovezzi, M.; Detlefs, B.; Ducotté, L. The five-analyzer point-to-point scanning crystal spectrometer at ESRF ID26. *J. Synchrotron Radiat.* **2021**, *28*, 362−371.
(63) Haverkort, M. W.; Zwierzycki, M.; Andersen, O. K. Multiplet ligand-field theory using Wannier orbitals. *Phys. Rev. B* **2012**, *85*, No. 165113.
(64) Retegan, M. Crispy, v0.7.3, Zenodo. 2019. DOI: 10.5281/zenodo.3258065. Accessed January 12, 2022.
(65) Glass, C. W.; Oganov, A. R.; Hansen, N. USPEX—Evolutionary crystal structure prediction. *Comput. Phys. Commun.* **2006**, *175*, 713−720.
(66) Oganov, A. R.; Lyakhov, A. O.; Valle, M. How Evolutionary Crystal Structure Prediction Works—and Why. *Acc. Chem. Res.* **2011**, *44*, 227−237.
(67) Lyakhov, A. O.; Oganov, A. R.; Stokes, H. T.; Zhu, Q. New developments in evolutionary structure prediction algorithm USPEX. *Comput. Phys. Commun.* **2013**, *184*, 1172−1182.
(68) Dovesi, R.; Erba, A.; Orlando, R.; Zicovich-Wilson, C. M.; Civalleri, B.; Maschio, L.; Rérat, M.; Casassa, S.; Baima, J.; Salustro, S.; Kirtman, B. Quantum-mechanical condensed matter simulations with CRYSTAL. *WIREs Comput. Mol. Sci.* **2018**, *8*, No. e1360.
(69) Erba, A.; Desmarais, J. K.; Casassa, S.; Civalleri, B.; Donà, L.; Bush, I. J.; Searle, B.; Maschio, L.; Edith-Daga, L.; Cossard, A.; et al. CRYSTAL23: A Program for Computational Solid State Physics and Chemistry. *J. Chem. Theory Comput.* **2023**, *19*, 6891−6932.
(70) Hourahine, B.; Aradi, B.; Blum, V.; Bonafé, F.; Buccheri, A.; Camacho, C.; Cevallos, C.; Deshaye, M. Y.; Dumitrică, T.; Dominguez, A.; et al. DFTB+, a software package for efficient

approximate density functional theory based atomistic simulations. *J. Chem. Phys.* **2020**, *152*, No. 124101.
(71) Kuklin, M. S.; Karttunen, A. J. Crystal Structure Prediction of Magnetic Transition-Metal Oxides by Using Evolutionary Algorithm and Hybrid DFT Methods. *J. Phys. Chem. C* **2018**, *122*, 24949−24957.
(72) Kuklin, M. S.; Karttunen, A. J. Evolutionary Algorithm-Based Crystal Structure Prediction of CuxZnyOz Ternary Oxides. *Molecules* **2023**, *28*, 5986.
(73) Bandemehr, J.; Baumann, D.; Seibald, M.; Eklund, K.; Karttunen, A. J.; Kraus, F. Mn(IV)-Substituted Metal(II) Hexafluorido Metallates(IV): Synthesis, Crystal Structures, and Luminescence Properties. *Eur. J. Inorg. Chem.* **2021**, *2021*, 3861−3869.
(74) Heiska, J.; Nisula, M.; Rautama, E.-L.; Karttunen, A. J.; Karppinen, M. Atomic/molecular layer deposition and electrochemical performance of dilithium 2-aminoterephthalate. *Dalton Trans.* **2020**, *49*, 1591−1599.
(75) Graham, A. J.; Banu, A.-M.; Düren, T.; Greenaway, A.; McKellar, S. C.; Mowat, J. P. S.; Ward, K.; Wright, P. A.; Moggach, S. A. Stabilization of Scandium Terephthalate MOFs against Reversible Amorphization and Structural Phase Transition by Guest Uptake at Extreme Pressure. *J. Am. Chem. Soc.* **2014**, *136*, 8606−8613.
(76) Carson, C. G.; Brunnello, G.; Lee, S. G.; Jang, S. S.; Gerhardt, R. A.; Tannenbaum, R. Structure Solution from Powder Diffraction of Copper 1,4-Benzenedicarboxylate. *Eur. J. Inorg. Chem.* **2014**, *2014*, 2140−2145.
(77) Chisca, D.; Croitor, L.; Petuhov, O.; Coropceanu, E. B.; Fonari, M. S. MOF-71 as a degradation product in single crystal to single crystal transformation of new three-dimensional Co(II) 1,4-benzenedicarboxylate. *CrystEngComm* **2016**, *18*, 38−41.
(78) Grimme, S.; Bannwarth, C.; Shushkov, P. A Robust and Accurate Tight-Binding Quantum Chemical Method for Structures, Vibrational Frequencies, and Noncovalent Interactions of Large Molecular Systems Parametrized for All spd-Block Elements (Z = 1−86). *J. Chem. Theory Comput.* **2017**, *13*, 1989−2009.
(79) Karttunen, A. J.; Tynell, T.; Karppinen, M. Atomic-Level Structural and Electronic Properties of Hybrid Inorganic−Organic ZnO:Hydroquinone Superlattices Fabricated by ALD/MLD. *J. Phys. Chem. C* **2015**, *119*, 13105−13114.
(80) Kuklin, M. S.; Eklund, K.; Linnera, J.; Ropponen, A.; Tolvanen, N.; Karttunen, A. J. Structural Properties and Magnetic Ground States of 100 Binary d-Metal Oxides Studied by Hybrid Density Functional Methods. *Molecules* **2022**, *27*, 874.
(81) Weigend, F.; Ahlrichs, R. Balanced basis sets of split valence, triple zeta valence and quadruple zeta valence quality for H to Rn: Design and assessment of accuracy. *Phys. Chem. Chem. Phys.* **2005**, *7*, 3297−3305.
(82) Pascale, F.; Zicovich-Wilson, C. M.; López Gejo, F.; Civalleri, B.; Orlando, R.; Dovesi, R. The calculation of the vibrational frequencies of crystalline compounds and its implementation in the CRYSTAL code. *J. Comput. Chem.* **2004**, *25*, 888−897.
(83) Zicovich-Wilson, C. M.; Pascale, F.; Roetti, C.; Saunders, V. R.; Orlando, R.; Dovesi, R. Calculation of the vibration frequencies of α-quartz: The effect of Hamiltonian and basis set. *J. Comput. Chem.* **2004**, *25*, 1873−1881.
(84) Maschio, L.; Kirtman, B.; Orlando, R.; Rèrat, M. Ab initio analytical infrared intensities for periodic systems through a coupled perturbed Hartree-Fock/Kohn-Sham method. *J. Chem. Phys.* **2012**, *137*, No. 204113.
(85) Maschio, L.; Kirtman, B.; Rérat, M.; Orlando, R.; Dovesi, R. Ab initio analytical Raman intensities for periodic systems through a coupled perturbed Hartree-Fock/Kohn-Sham method in an atomic orbital basis. II. Validation and comparison with experiments. *J. Chem. Phys.* **2013**, *139*, No. 164102.
(86) 84"CRYSPLOT: A modern and easy to use visualization environment for plotting properties of crystalline solids as computed by means of the CRYSTAL code found under http://crysplot.crystalsolutions.eu/index.html, 2022.
(87) Philip, A.; Vasala, S.; Glatzel, P.; Karppinen, M. Atomic/molecular layer deposition of Ni-terephthalate thin films. *Dalton Trans.* **2021**, *50*, 16133−16138.
(88) Coates, J. Interpretation of Infrared Spectra, A Practical Approach. In *Encyclopedia of Analytical Chemistry*; Meyers, R. A., Ed.; John Wiley & Sons Ltd: Chichester, U.K., 2000; pp 10815−10837.
(89) Nguyen, D. T. C.; Le, H. T. N.; Do, T. S.; Pham, V. T.; Lam Tran, D.; Ho, V. T. T.; Tran, T. V.; Nguyen, D. C.; Nguyen, T. D.; Bach, L. G.; et al. Metal-organic framework MIL-53(Fe) as an adsorbent for ibuprofen drug removal from aqueous solutions: response surface modeling and optimization. *J. Chem.* **2019**, *2019*, No. 5602957.
(90) Bordiga, S.; Lamberti, C.; Ricchiardi, G.; Regli, L.; Bonino, F.; Damin, A.; Lillerud, K. P.; Bjorgen, M.; Zecchina, A. Electronic and vibrational properties of a MOF-5 metal−organic framework: ZnO quantum dot behaviour. *Chem. Commun.* **2004**, 2300−2301.
(91) Bronstein, L. M.; Huang, X.; Retrum, J.; Schmucker, A.; Pink, M.; Stein, B. D.; Dragnea, B. Influence of Iron Oleate Complex Structure on Iron Oxide Nanoparticle Formation. *Chem. Mater.* **2007**, *19*, 3624−3632.
(92) Lu, Y.; Miller, J. D. Carboxyl Stretching Vibrations of Spontaneously Adsorbed and LB-Transferred Calcium Carboxylates as Determined by FTIR Internal Reflection Spectroscopy. *J. Colloid Interface Sci.* **2002**, *256*, 41−52.
(93) Ahvenniemi, E.; Karppinen, M. ALD/MLD processes for Mn and Co based hybrid thin films. *Dalton Trans.* **2016**, *45*, 10730−10735.
(94) Asheghhosseini, A.; Zolgharnein, J. Iron terephthalate metal−organic framework (MOF-235) as an efficient adsorbent for removal of toluidine blue dye from aqueous solution using Box−Behnken design as multivariate optimization approach. *J. Iran. Chem. Soc.* **2020**, *17*, 2663−2673.
(95) Rowsell, J. L. C.; Yaghi, O. M. Metal−organic frameworks: a new class of porous materials. *Microporous Mesoporous Mater.* **2004**, *73*, 3−14.
(96) Nguyen, V. H.; Nguyen, T. D.; Bach, L. G.; Hoang, T.; Bui, Q. T.; Tran, L. D.; Nguyen, C. V.; Vo, D.-V. N.; Do, S. T. Effective Photocatalytic Activity of Mixed Ni/Fe-Base Metal-Organic Framework under a Compact Fluorescent Daylight Lamp. *Catalysts* **2018**, *8*, 487.
(97) Mai, S.; Klingler, S.; Trentin, I.; Kund, J.; Holzer, M.; Andreeva, A.; Stach, R.; Kranz, C.; Streb, C.; Mizaikoff, B.; González, L. Spectral Signatures of Oxidation States in a Manganese-Oxo Cubane Water Oxidation Catalyst. *Chem. Eur. J.* **2021**, *27*, 17078−17086.
(98) de Groot, F. M. F.; Glatzel, P.; Bergmann, U.; van Aken, P. A.; Barrea, R. A.; Klemme, S.; Hävecker, M.; Knop-Gericke, A.; Heijboer, W. M.; Weckhuysen, B. M. 1s2p Resonant Inelastic X-ray Scattering of Iron Oxides. *J. Phys. Chem. B* **2005**, *109*, 20751−20762.
(99) Bergmann, U.; Glatzel, P. X-ray emission spectroscopy. *Photosynth. Res.* **2009**, *102*, 255−266.
(100) Glatzel, P.; Bergmann, U.; Yano, J.; Visser, H.; Robblee, J. H.; Gu, W.; de Groot, F. M. F.; Christou, G.; Pecoraro, V. L.; Cramer, S. P.; Yachandra, V. K. The Electronic Structure of Mn in Oxides, Coordination Complexes, and the Oxygen-Evolving Complex of Photosystem II Studied by Resonant Inelastic X-ray Scattering. *J. Am. Chem. Soc.* **2004**, *126*, 9946−9959.
(101) Medina, M. E.; Dumont, Y.; Grenèche, J.-M.; Millange, F. FeIII/FeII regular charge order in metal−organic framework. *Chem. Commun.* **2010**, *46*, 7987−7989.
(102) Sun, Q.; Liu, M.; Li, K.; Han, Y.; Zuo, Y.; Wang, J.; Song, C.; Zhang, G.; Guo, X. Controlled synthesis of mixed-valent Fe-containing metal organic frameworks for the degradation of phenol under mild conditions. *Dalton Trans.* **2016**, *45*, 7952−7959.
(103) Tanskanen, A.; Mustonen, O.; Karppinen, M. Simple ALD process for ε-Fe2O3 thin films. *APL Mater.* **2017**, *5*, No. 056104.
(104) Jussila, T.; Philip, A.; Lindén, J.; Karppinen, M. High-quality magnetically hard ε-Fe2O3 thin films through atomic layer deposition for room-temperature applications. *Adv. Eng. Mater.* **2023**, *25*, No. 2201262.

https://doi.org/10.1021/acs.chemmater.4c00555
Chem. Mater. 2024, 36, 6489−6503

(105) Tamm, A.; Tarre, A.; Kozlova, J.; Rähn, M.; Jõgiaas, T.; Kahro, T.; Link, J.; Stern, R. Atomic layer deposition of superparamagnetic ruthenium-doped iron oxide thin film. *RSC Adv.* **2021**, *11*, 7521−7526.
(106) Kalam, K.; Otsus, M.; Kozlova, J.; Tarre, A.; Kasikov, A.; Rammula, R.; Link, J.; Stern, R.; Vinuesa, G.; Lendínez, J. M. Memory effects in nanolaminates of hafnium and iron oxide films structured by atomic layer deposition. *Nanomaterials* **2022**, *12*, 2593.
(107) Aronniemi, M.; Saino, J.; Lahtinen, J. Characterization and gas-sensing behavior of an iron oxide thin film prepared by atomic layer deposition. *Thin Solid Films* **2008**, *516*, 6110−6115.
(108) Richey, N. E.; de Paula, C.; Bent, S. F. Understanding chemical and physical mechanisms in atomic layer deposition. *J. Chem. Phys.* **2020**, *152*, No. 040902.
(109) Li, J.; Chai, G.; Wang, X. Atomic layer deposition of thin films: from a chemistry perspective. *Int. J. Extreme Manuf.* **2023**, *5*, No. 032003.
(110) Raphael Karikachery, A.; Lee, H. B.; Masjedi, M.; Ross, A.; Moody, M. A.; Cai, X.; Chui, M.; Hoff, C. D.; Sharp, P. R. High Quantum Yield Molecular Bromine Photoelimination from Mononuclear Platinum(IV) Complexes. *Inorg. Chem.* **2013**, *52*, 4113−4119.
(111) Carrera, E. I.; McCormick, T. M.; Kapp, M. J.; Lough, A. J.; Seferos, D. S. Thermal and Photoreductive Elimination from the Tellurium Center of π-Conjugated Tellurophenes. *Inorg. Chem.* **2013**, *52*, 13779−13790.
(112) Clausen, H. F.; Poulsen, R. D.; Bond, A. D.; Chevallier, M.-A. S.; Iversen, B. B. Solvothermal synthesis of new metal organic framework structures in the zinc−terephthalic acid−dimethyl formamide system. *J. Solid State Chem.* **2005**, *178*, 3342−3351.
(113) Steele, J. A.; Solano, E.; Hardy, D.; Dayton, D.; Ladd, D.; White, K.; Chen, P.; Hou, J.; Huang, H.; Saha, R. A.; et al. How to GIWAXS: Grazing Incidence Wide Angle X-Ray Scattering Applied to Metal Halide Perovskite Thin Films. *Adv. Energy Mater.* **2023**, *13*, No. 2300760.
(114) Momma, K.; Izumi, F. VESTA 3 for three-dimensional visualization of crystal, volumetric and morphology data. *J. Appl. Crystallogr.* **2011**, *44*, 1272−1276.
(115) Le, T. D.; Nguyen, K. D.; Nguyen, V. T.; Truong, T.; Phan, N. T. S. 1,5-Benzodiazepine synthesis via cyclocondensation of 1,2-diamines with ketones using iron-based metal−organic framework MOF-235 as an efficient heterogeneous catalyst. *J. Catal.* **2016**, *333*, 94−101.
(116) Makhanya, N. P.; Oboirien, B.; Musyoka, N.; Ren, J.; Ndungu, P. Evaluation of PET-derived metal organic frameworks (MOFs) for water adsorption and heat storage. *J. Porous Mater.* **2023**, *30*, 387−401.
(117) Huo, S.-H.; Yan, X.-P. Metal−organic framework MIL-100(Fe) for the adsorption of malachite green from aqueous solution. *J. Mater. Chem.* **2012**, *22*, 7449−7455.
(118) Kulal, P. M.; Dubal, D. P.; Lokhande, C. D.; Fulari, V. J. Chemical synthesis of Fe2O3 thin films for supercapacitor application. *J. Alloys Compd.* **2011**, *509*, 2567−2571.

https://doi.org/10.1021/acs.chemmater.4c00555
Chem. Mater. 2024, 36, 6489−6503